Transient Synchronization Stability Analysis and Assessment of DFIG System Under Severe Faults

Hongsheng Xu and Meng Zhan, *Senior Member, IEEE*

***Abstract*—In the transient stability analysis of renewable energy grid-tied systems, although a large amount of works have been devoted to the detailed electromagnetic transient simulation and the stability analyses of during-fault stage, the whole low-voltage ride through (LVRT) process and transient stability mechanism remain to be uncovered. Taking the doubly fed induction generator (DFIG) system as an objective, this article divides its transient processes into four different stages, including the prefault, during-fault, early postfault, and late postfault ones, establishes the full mechanism models for each stage, and studies the sequential switching dynamics in detail. It is found that the during-fault dynamics can be determined by the phase-lock loop second-order equation within the framework of the generalized swing equation (GSE), with additive scaled parameters. In particular, for the early postfault stage dynamics, it can be treated as a series of quasisteady states and its dominant driving system dynamics can still be described by the GSE. Thus the system transient stability can be completely determined by whether the initial state of the early postfault stage is within or out of its corresponding basin of attraction (BOA). Based on these unique dynamical characteristics, the BOA-based and equal area criterion-based transient stability assessment methods are developed, which are supported by broad numerical simulations and hardware-in-the-loop experiments. This work provides a clear physical picture and perfectly solves the difficult stability analysis problem when severe faults and LVRT showing discontinuous switching dynamics have to be considered in most of DFIG engineering situations.**

***Index Terms*—Basin of attraction (BOA), doubly fed induction generator (DFIG), equal area criterion (EAC), low-voltage ride through (LVRT), transient synchronization stability.**

NOMENCLATURE

$\boldsymbol{U}_t, \boldsymbol{I}_t, \boldsymbol{U}_g$	Terminal voltage and output current and grid voltage vectors.
$\boldsymbol{I}_s, \boldsymbol{I}_r, \boldsymbol{I}_c$	Stator current, rotor current and grid converter output current.
U_t, U_g	Amplitude of terminal voltage and grid voltage.
i_{td}, i_{tq}	dq axis components of output current of DFIG.
u_{td}, u_{tq}	dq axis components of terminal voltage.
θ_{pll}	Phase-locked loop (PLL) output angle in three-phase stationary abc reference frame.
φ_{pll}	PLL output angle in xy common reference frame.
φ_{cr}	Critical clearing angle.
k_{pw}, k_{iw}	PI parameters of RSC.
k_{pV}, k_{iV}	PI parameters of TVC.
$k_{p\text{pll}}, k_{i\text{pll}}$	PI parameters of PLL.
K_e, K_{ramp}	Reactive current ratio coefficient and ramp rate.
P_t, Q_t	Output active power and reactive power of DFIG.
ω_0	Rotation speed of xy common reference frame.
$\omega_{\text{pll}}, \omega_g, \omega_r$	Frequencies of PLL, grid, and rotor speed, respectively.
X_m, X_s, X_g	Mutual reactance, stator reactance, and grid reactance.
a, b, c, d	Correction coefficients.
$\mathbf{x}_s, \mathbf{x}_u$	Stable and unstable equilibrium points.
$P_m, P_e, M_{\text{eq}}, D_{\text{eq}}$	Equivalent mechanical power, electromagnetic power, inertia, and damping, respectively.
t_f, t_c, t_r	Times for the fault occurrence, clearing, and ramp-ending, respectively.
1,2,3,4	Subscripts of stages 1, 2, 3, and 4, for prefault, during-fault, early postfault, and late post-fault, respectively.

Received 25 July 2025; accepted 28 August 2025. Date of publication 2 September 2025; date of current version 23 December 2025. This work was supported by the National Natural Science Foundation of China under Grant U22B6008. Recommended for publication by Associate Editor D. S. Oliveira. *(Corresponding author: Meng Zhan.)*

The authors are with the State Key Laboratory of Advanced Electromagnetic Engineering and Technology, Hubei Electric Power Security and High Efficiency Key Laboratory, School of Electrical and Electronic Engineering, Huazhong University of Science and Technology, Wuhan 430074, China (e-mail: xhs@hust.edu.cn; zhanmeng@hust.edu.cn).

Color versions of one or more figures in this article are available at https://doi.org/10.1109/TPEL.2025.3605030.

Digital Object Identifier 10.1109/TPEL.2025.3605030

I. INTRODUCTION

IN recent years, doubly fed induction generator (DFIG) has become a mainstream renewable energy equipment in power systems [1]. Compared to the synchronous generator (SG), the DFIG exhibits insufficient overcurrent capacity under severe faults, and many countries have developed grid codes for the operation of DFIG to avoid its off-grid [2], [3]. Based on these grid codes, the DFIG should experience multiple switching processes during the low-voltage ride through (LVRT). The relevant transient synchronous stability (TSS) analysis and assessment has become a hot topic [4], [5], [6].

In the general sequential switching schemes, the LVRT can be divided into four stages: prefault (stage 1), during-fault

(stage 2), early postfault (stage 3), and late postfault (stage 4) [3]. The DFIG has to implement corresponding controls at each stage to meet different requirements. In stages 1 and 4, normal control is employed to ensure stability [7]. In stage 2, the DFIG needs to switch to the LVRT control to quickly support terminal voltage [8]. In stage 3, the ramp (climbing) control is employed to limit the active power recovery speed [3]. Considering the complete LVRT processes, the system exhibits high-dimensional, nonlinear, and event-driving switch characteristics. Usually the switching system analysis, which involves the full-stage dynamics, is extremely difficult.

Under the during-fault stage 2, it is found that the hardware protection circuit and the ac current control dynamics can be ignored and the phase-lock loop (PLL) dynamics for synchronizing with the grid is important. Under this situation, the system can be simplified as a second-order system. If the system loses its equilibrium point during the fault, a phenomenon of loss of synchronism is reported [9]. Due to its structural similarity with the swing equation of the SG, it is called generalized swing equation (GSE) [10], [11], [12]. So far, some classical analytical methods including the Lyapunov method [13], equal area criterion (EAC) method [14], phase portrait approach [15], and perturbation method [16], etc., are widely developed. In addition, taking into account saturation nonlinearities, more complicated nonlinear dynamical behaviors are reported very recently [17], [18]. However, it should be notable that the during-fault stage is only a fraction of the whole LVRT processes, and strictly the system stability should be judged after all four stages, based on the dynamical system theory.

Obviously the active power recovery stage 3 in the LVRT is also important [19], [20]. So far, transient stability analysis considering the dynamics of stage 3 mainly relies on electromagnetic transient (EMT) simulation. The generic models proposed by WECC and GE have been widely applied in simulation tests [21], [22]. They take into account very detailed aspects, including numerous modules such as the switching tube, limit, and delay. However, they are difficult for stability mechanism analysis. A mechanism model catching dominant dynamics is helpful and expected. Except these studies, after greatly simplifying the dynamics of LVRT, the stability influence of the DFIG on the rotor angle of SG in the hybrid systems has been studied [23], [24]. These studies usually regard SG as the main body in the transient synchronization stability and consider renewable equipment merely as a (steady-state) power source. However, during the complete LVRT processes, renewable equipment may still pose transient stability risks. In recent studies [25], [26], [27], several transient models considering the complete LVRT processes are constructed, and the TSS analysis is no longer limited to stage 2. However, in the whole LVRT processes, which stage is the most critical still needs to be studied. In addition, as stage 3 exhibits nonautonomous characteristics, detailed dynamical property of stage 3 and its impact on the transient stability remain to be studied.

Therefore, this article aims to provide a system-level physical picture of the DFIG grid-tied system by considering the complete LVRT processes, analyze the dominant factors and physical mechanism for the TSS, and develop novel TSS assessment methods. The main contributions in terms of modeling, analysis, and assessment are as follows.

1) In the transient modeling contribution, a transient reduced-order model with scaled parameters is constructed for each stage, to uncover the dominant dynamical characteristics and clarify switching conditions.
2) In the dynamics analysis contribution, the bulk dynamics in both stages 2 and 3 can be caught by the GSE, the initial state of stage 3 plays a decisive role, and the TSS can be completely determined by the condition if it is within or out of the basin of attraction (BOA) of the beginning of stage 3.
3) In the stability assessment contribution, two efficient BOA-based and EAC-based methods are proposed. The TSS can be assessed immediately at the initial moment of stage 3. Both methods exhibit perfect results.

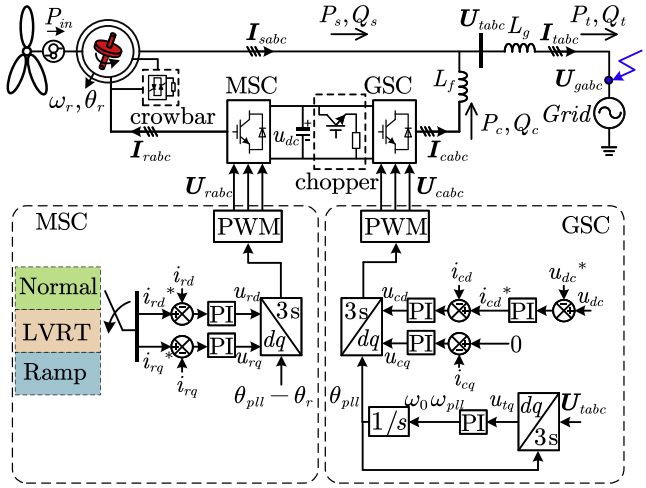

Fig. 1. Schematic show of the DFIG system considering LVRT.

The rest of this article is organized as follows. In Section II, the topology structure and sequential switching characteristics of the DFIG system are introduced. In Section III, the transient mechanism model is constructed for all four stages. In Section IV, an EAC-based assessment method for permanent voltage-dip faults is introduced, as most of previous researchers have studied. In Section V, by studying the dynamical characteristics in stage 3, the salient effect of its initial state is uncovered. In Section VI, a novel EAC assessment method is developed and the influence mechanism of parameters is analyzed. In Section VII, the theoretical and simulation results are widely verified by experiments. Finally, Section VIII concludes this article are made. In addition, a detailed full-order DFIG model is given in Appendix B.

II. DFIG System Considering LVRT

The topology structure and control scheme of the DFIG system are shown in Fig. 1. Various types of energy storage element are included, such as the ac inductor, dc capacitor, and mechanical rotor, and the different dynamical responses of these elements are attributed to their own storage capacities.

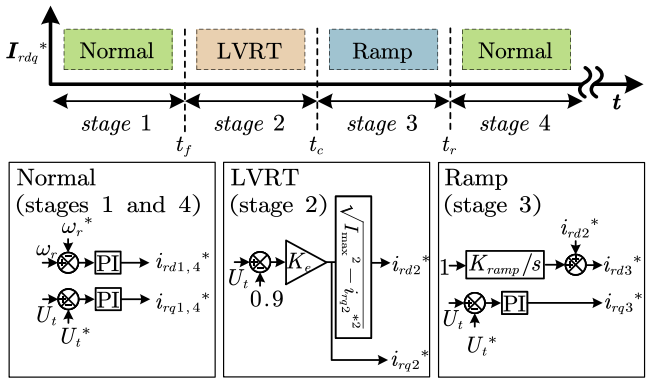

Fig. 2. Schematic shows of typical switching controls under different stages, including stages 1 (prefault) and 4 (late postfault) for the normal control, stage 2 (during-fault) for the LVRT control, and stage 3 (early postfault) for the ramp control. t_f, t_c, and t_r denote the times for the fault occurrence, clearing, and ramp-ending, respectively. Throughout this article, the subscripts 1, 2, 3, and 4 are used to denote the corresponding stages.

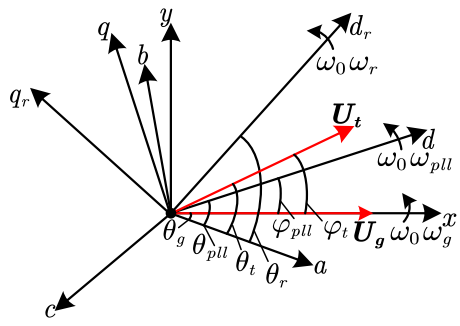

Fig. 3. Schematic shows of three-phase stationary abc reference frame, xy reference frame, dq common reference frame, and rotor reference frame, where $\omega_0\omega_g$, $\omega_0\omega_{\text{pll}}$, and $\omega_0\omega_r$ represent the rotation angular frequencies of the xy, dq, and rotor reference frames, respectively. $\omega_0 = 2\pi f_0$.

Correspondingly, the cascaded controllers adopt matched bandwidths to control these elements. For example, the bandwidth of the inner loop should be designed about ten times larger than that of the outer loop.

There are various types of faults in the power system. The DFIG takes corresponding protective measures according to different types of faults. If the terminal voltage U_t of the DFIG drops below a certain target value, the LVRT control will be activated. In this case, we usually consider the fault to be severe [28]. On the contrary, the fault is believed as shallow, if the LVRT control is not activated [28]. In addition, in this article, we adopt a typical symmetrical voltage sag fault, which widely occurs in transient disturbances [29]. According to the grid code in China, when the terminal voltage U_t of DFIG is lower than 0.8 p.u., the LVRT control needs to be switched on [3]. During the LVRT processes, the crowbar and chopper are triggered to protect the converter and capacitor. If the fault is small under the shallow fault, the DFIG maintains the normal control, as shown in Fig. 1. For the grid-side converter (GSC), it is composed of the dc-voltage control (DVC) and the ac current control. The DVC aims to maintain the dc-voltage stable. The reactive power branch is to control the power factor, and usually the reference current i_{cq}^* is set to zero, i.e., $i_{cq}^* = 0$ [30]. For the machine-side converter (MSC), it includes the maximum power point tracking control, pitch control, rotor speed control (RSC), terminal voltage control (TVC), and ac current control. Since the maximum power point tracking and the pitch controls exhibit a comparatively slow performance, they are ignored in this article. The RSC aims to keep rotor speed stable, and the TVC aims to ensure the terminal voltage stable.

Under a severe fault, the LVRT should be switched on according to the sequential switching schemes, as shown in Fig. 1. In particular, the outer loop control of the MSC should vary under different stages, as shown in Fig. 2. Moreover, in the latest research [31], the role of the outer loop and the PLL during the LVRT processes is considered to be significant. This viewpoint will be highlighted in our modeling part. The control and switching conditions for each stage will be studied in detail afterwards. Here, t_f, t_c, and t_r denote the times for the fault occurrence, clearing, and ramp-ending, respectively. Throughout this article, the subscripts 1, 2, 3, and 4 are used to denote the corresponding stages.

To unify coordinate of variables, the variables of the GSC and the MSC prompt the dq reference frame provided by the PLL. Fig. 3 shows the relationships between these different reference frames, where the phase mismatch of the rotating vector relative to the xy reference frame is denoted by φ. For example, $\varphi_{\text{pll}} = \theta_{\text{pll}} - \omega_0\omega_g t$. For the fundamental angular frequency, $\omega_0 = 2\pi f_0$, and for the grid angular frequency, $\omega_g = 1$ p.u..

III. Transient Different-Stage Model Considering LVRT Processes

To catch the dominant dynamics and focus on the core factor of the TSS, we only keep the slowest scale dynamics plus the PLL which are the most important, under the following assumptions.

1) The fast dynamics of the inductance, including the line inductance L_g, stator inductance L_s, and rotor inductance L_r, are neglected. Given that the response speed of the ac current control is very fast, its dynamics is also ignored, and thus $i_{rd} = {i_{rd}}^*, i_{rq} = {i_{rq}}^*, i_{cd} = {i_{cd}}^*$, and $i_{cq} = {i_{cq}}^*$.
2) According to the grid code of China, it is mandatory to switch into the LVRT control within 60 ms under severe faults [3]. Therefore, the operating time of the crowbar and demagnetization control is extremely brief and can be ignored. In addition, the overheating limit of the chopper is neglected.
3) The GSC is considered as a controlled current source and its dynamics is ignored. Hence the output current i_{cd} of the GSC is in a slip multiple relationship with the stator current i_{sd}: $i_{cd} = -s_p i_{sd}$. Here, the slip ratio $s_p = (\omega_g - \omega_r)/\omega_g$. ω_g is the per-unit value of grid-side frequency, which is approximately considered as $\omega_g \approx 1$. Thus, $i_{cd} = (\omega_r - 1)i_{sd}$.

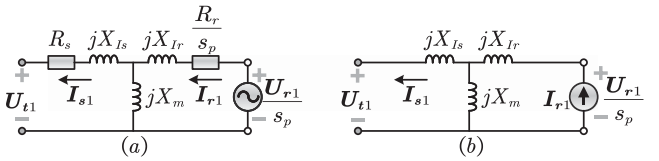

Fig. 4. Quasisteady-state topological circuit of asynchronous machine in the DFIG. Here, X_{Is}, X_{Ir}, and X_m are the per-unit values of leakage stator reactance, leakage rotor reactance, and mutual inductance reactance, respectively. For the stator reactance X_s, $X_s = X_{Is} + X_m$, and for the rotor reactance X_r, $X_r = X_{Ir} + X_m$. (a) represents the equivalent circuit diagram considering the resistance of the stator and rotor and the dynamics of the inner loop and (b) represents the equivalent circuit diagram ignoring the resistance of the stator and rotor and the dynamics of the inner loop.

A. Stage 1: Prefault

The detailed full-order model in stage 1 is shown in Appendix B and summarized in (B.19) and (B.20), as a reference. To analyze the TSS mechanism effectively, we will obtain the reduced-order mechanism model first.

First, due to the rapid dynamics of the magnetic flux linkage, the quasisteady-state assumption of the magnetic flux linkage is usually adopted in practical analysis [32]. In the dynamic expression of the flux linkage (B.2) in Appendix B, by setting the differential terms in (B.2) to zero and combining it with (B.3), we can obtain the algebraic relationship between the voltages and currents of the stator and rotor as follows:

$$\begin{cases} u_{rd1}/s_p = i_{rd1}R_r/s_p - X_r i_{rq1} + X_m i_{sq1} \\ u_{rq1}/s_p = i_{rq1}R_r/s_p + X_r i_{rd1} - X_m i_{sd1} \\ u_{td1} = -R_s i_{sd1} + X_s i_{sq1} - X_m i_{rq1} \\ u_{tq1} = -R_s i_{sq1} - X_s i_{sd1} + X_m i_{rd1} \end{cases} \tag{1}$$

where the stator reactance $X_s = X_{Is} + X_m$, and the rotor reactance $X_r = X_{Ir} + X_m$.

The corresponding quasisteady-state topological circuit is shown in Fig. 4(a). Here, the rotor voltage $\boldsymbol{U}_{r1}$ and rotor resistance R_r are converted to the stator side, so they are divided by slip ratio s_p on the basis of the original values.

Second, in the MSC, the ac current control has a very fast dynamic response, which decays rapidly. Since the problem studied in this article focuses on the dynamic behavior of the slowest scale, it is assumed that the rotor current can always follow the command value

$$\begin{cases} i_{rd1} = {i_{rd1}}^* \\ i_{rq1} = {i_{rq1}}^*. \end{cases} \tag{2}$$

This means that the rotor voltage source in Fig. 4(a) can be replaced by a rotor current source. In addition, since the stator and rotor resistances are usually very small and are generally neglected, the quasisteady-state topological circuit of the asynchronous machine can be transformed from Fig. 4(a)–(b), and (1) can be further transformed to

$$\begin{cases} u_{rd1}/s_p = -X_r i_{rq1} + X_m i_{sq1} \\ u_{rq1}/s_p = X_r i_{rd1} - X_m i_{sd1} \\ u_{td1} = X_s i_{sq1} - X_m i_{rq1} \\ u_{tq1} = -X_s i_{sd1} + X_m i_{rd1}. \end{cases} \tag{3}$$

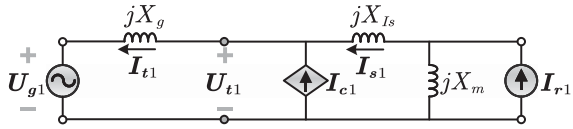

Fig. 5. Equivalent topology circuit of DFIG grid-connected system.

Third, compared with the dynamics of the MSC, the branch of GSC is still fast. The output power of GSC accounts for 20%–30%, and it has a relatively minor impact on the stability of the system. Therefore, the branch of GSC is usually regarded as a controlled current source [7], [31], and the relationship between its output current $\boldsymbol{I}_{c1}$ and the stator current $\boldsymbol{I}_{s1}$ is as follows:

$$\begin{cases} i_{cd1} = (\omega_{r1} - 1) i_{sd1} \\ i_{cq1} = 0. \end{cases} \tag{4}$$

Eventually, as shown in Fig. 5, we can obtain the equivalent topological circuit of the DFIG grid-connected system. The topological circuits of other stages are the same, with only differences in the number subscripts.

According to Fig. 5, the total output currents $\boldsymbol{I}_{t1}$ of the DFIG in the dq-axis are

$$\begin{cases} i_{td1} = i_{sd1} + i_{cd1} \\ i_{tq1} = i_{sq1} + i_{cq1}. \end{cases} \tag{5}$$

Combining (4) and (5), we can obtain the relation between $\boldsymbol{I}_{t1}$ and $\boldsymbol{I}_{s1}$ as

$$\begin{cases} i_{td1} = \omega_{r1} i_{sd1} \\ i_{tq1} = i_{sq1}. \end{cases} \tag{6}$$

As the transmission line dynamics are ignored, the relationship between the terminal voltage $\boldsymbol{U}_{t1}$ and the current $\boldsymbol{I}_{t1}$ is described by

$$\begin{cases} u_{td}1 = U_{g1} \cos \varphi_{\text{pll}1} - X_g i_{tq1} \\ u_{tq}1 = -U_{g1} \sin \varphi_{\text{pll}1} + X_g i_{td1}. \end{cases} \tag{7}$$

Combining (6), (7), and the last two equations of (3) for the relation between $\boldsymbol{U}_{t1}$, $\boldsymbol{I}_{s1}$, and $\boldsymbol{I}_{r1}$, through eliminating $\boldsymbol{I}_{s1}$ (i_{sd1}/i_{sq1}), an explicit relation between $\boldsymbol{U}_{t1}$ and $\boldsymbol{I}_{r1}$ is obtained as

$$\begin{cases} u_{td}1 = aU_{g1} \cos \varphi_{\text{pll}1} - bX_g i_{rq1} \\ u_{tq}1 = -cU_{g1} \sin \varphi_{\text{pll}1} + dX_g i_{rd1} \end{cases} \tag{8}$$

where the correction coefficients (a, b, c, and d) are

$$\begin{cases} a = X_s/(X_s + X_g) \\ b = X_m/(X_s + X_g) \\ c = X_s/(X_s + \omega_{r1} X_g) \\ d = \omega_{r1} X_m/(X_s + \omega_{r1} X_g). \end{cases} \tag{9}$$

The rotor speed ω_r is nearly unchanged within the short duration time of the LVRT process, and all these correction coefficients can be regarded as constants, based on $\omega_{r1} = {\omega_{r1}}^*$ for the stable equilibrium point (SEP) in (9). For example, under the system parameters listed in Appendix A, $a = 0.89$, $b = 0.85$, $c = 0.87$, and $d = 1$ are obtained and fixed for all four stages. Therefore, here $\boldsymbol{U}_{t1}$ and $\boldsymbol{I}_{r1}$ show the only difference of these scaled, correction coefficients, to be compared with the original relation between $\boldsymbol{U}_{t1}$ and $\boldsymbol{I}_{t1}$ in (7). As we will see, (8) and (9)

establish the direct relation between the terminal voltage $\boldsymbol{U}_{t1}$ and the controlled rotor current $\boldsymbol{I}_{r1}$ and are very important.

In addition, combining (6) and the last two equations of (3), the relationship between $\boldsymbol{I}_{t1}$ and $\boldsymbol{I}_{r1}$ becomes

$$\begin{cases} i_{td}1 = \omega_{r1}(X_m i_{rd}1 - u_{tq1})/X_s \\ i_{tq}1 = (X_m i_{rq}1 + u_{td1})/X_s. \end{cases} \tag{10}$$

Thus, the output power P_{t1} and the amplitude of the terminal voltage U_{t1} are

$$\begin{cases} P_{t1} = u_{td}1 i_{td}1 + u_{tq}1 i_{tq}1 \\ U_t 1 = \sqrt{{u_{td1}}^2 + {u_{tq1}}^2}. \end{cases} \tag{11}$$

Since the equivalent topological circuit of Fig. 5 is applicable in all stages, the network algebraic relations (8), (10), and (11) are also the same. According to Fig. 2, different controls will be adopted at different stages to change the rotor current source in Fig. 5.

In stage 1, the DFIG adopts the normal control. For the MSC, the typical proportional–integral (PI) control is adopted in the RSC and TVC, whose differential equations are

$$\begin{cases} \dot{i}_{rd1} = k_{pw}\dot{\omega}_{r1} + k_{iw}\left(\omega_{r1} - {\omega_r}^*\right) \\ \dot{i}_{rq1} = k_{pV}\dot{U}_{t1} + k_{iV}\left(U_{t1} - {U_t}^*\right) \end{cases} \tag{12}$$

where k_{pw} and k_{iw} are the proportional and integral coefficients of the RSC, respectively, k_{pV} and k_{iV} are the proportional and integral coefficients of the TVC, respectively, and ${\omega_r}^*$ and ${U_t}^*$ are the reference values of the rotor speed and the terminal voltage, respectively.

The motion equation of the rotor is

$$\dot{\omega}_{r1} = \frac{P_{\text{in}} - P_{t1}}{2H\omega_{r1}} \tag{13}$$

where H represents the inertial time constant. P_{in} and P_{t1} represent the mechanical input power and the electromagnetic output power, respectively.

For the PLL dynamics, the relation between $\omega_{\text{pll}1}$ and the integrator output $x_{\text{pll}1}$ is $\omega_0\omega_{\text{pll}1} = \omega_0 x_{\text{pll}1} + k_{p\text{pll}}u_{tq1}$, and the corresponding differential equations are

$$\begin{cases} \dot{x}_{\text{pll}1} = (k_{i\text{pll}}u_{tq1})/\omega_0 \\ \dot{\varphi}_{\text{pll}1} = \omega_0((k_{p\text{pll}}u_{tq1})/\omega_0 + x_{\text{pll}1} - 1) \end{cases} \tag{14}$$

where $k_{p\text{pll}}$ and $k_{i\text{pll}}$ are the proportional and integral coefficients of the PLL, respectively.

Finally, the differential–algebraic equations (DAEs) in stage 1 including the major dynamics of the RSC, TVC, PLL, and rotor are

$$\begin{cases} \dot{\omega}_{r1} = (P_{\text{in}} - P_{t1})/(2H\omega_{r1}) \\ \dot{i}_{rd1} = k_{pw}\dot{\omega}_{r1} + k_{iw}(\omega_{r1} - {\omega_r}^*) \\ \dot{i}_{rq1} = k_{pV}\dot{U}_{t1} + k_{iV}(U_{t1} - {U_t}^*) \\ \dot{x}_{\text{pll}1} = (k_{i\text{pll}}u_{tq1})/\omega_0 \\ \dot{\varphi}_{\text{pll}1} = \omega_0((k_{p\text{pll}}u_{tq1})/\omega_0 + x_{\text{pll}1} - 1) \end{cases} \tag{15}$$

$$\begin{cases} u_{td}1 = aU_{g1}\cos\varphi_{\text{pll}1} - bX_g i_{rq1} \\ u_{tq}1 = -cU_{g1}\sin\varphi_{\text{pll}1} + dX_g i_{rd1} \\ i_{td}1 = \omega_{r1}(X_m i_{rd}1 - u_{tq1})/X_s \\ i_{tq}1 = (X_m i_{rq}1 + u_{td1})/X_s \\ P_{t1} = u_{td}1 i_{td}1 + u_{tq}1 i_{tq}1 \\ U_t 1 = \sqrt{{u_{td1}}^2 + {u_{tq1}}^2}. \end{cases} \tag{16}$$

When the system is in a steady state, $u_{td}1 = {U_t}^*$, $u_{tq}1 = 0$, and $P_{t1} = P_{in} = i_{td}1{U_t}^*$. Thus, there exist an SEP, $\mathbf{x}_s$

$$\begin{cases} \omega_{r1,s} = {\omega_r}^* \\ i_{rd1,s} = \frac{X_s P_{\text{in}}}{X_m {\omega_r}^*} \\ i_{rq1,s} = \frac{X_s U_{g1}\cos\varphi_{\text{pll}1,s} - (X_s + X_g){U_t}^*}{X_g X_m} \\ x_{pll1,s} = 1 \\ \varphi_{\text{pll}1,s} = \arcsin\left(\frac{P_{\text{in}}X_g}{U_{g1}{U_t}^*}\right) \end{cases} \tag{17}$$

and an unstable equilibrium point (UEP), $\mathbf{x}_u$

$$\begin{cases} \omega_{r1,u} = {\omega_r}^* \\ i_{rd1,u} = \frac{X_s P_{\text{in}}}{X_m {\omega_r}^*} \\ i_{rq1,u} = \frac{X_s U_{g1}\cos\varphi_{\text{pll}1,u} - (X_s + X_g){U_t}^*}{X_g X_m} \\ x_{\text{pll}1,u} = 1 \\ \varphi_{\text{pll}1,u} = \pi - \arcsin\left(\frac{P_{\text{in}}X_g}{U_{g1}{U_t}^*}\right). \end{cases} \tag{18}$$

Under the typical parameters in Appendix A, $\mathbf{x}_s = [1.2, 0.7, -0.43, 1, 0.41]^T$ p.u. and $\mathbf{x}_u = [1.2, 0.7, -4.25, 1, 2.73]^T$ p.u., where the superscript T denotes transposition. Clearly $\mathbf{x}_s$ provides an initial stable operating point for the sequential stages.

B. Stage 2: During-Fault

When a severe fault occurs, e.g., U_g dips from 1.0 p.u. to a much smaller U_{g2}, the terminal voltage U_{t2} dips below 0.8 p.u. accordingly, causing the normal control to freeze. Stage 2 begins. Now the dq current of the MSC is provided by the LVRT control. To rapidly support U_{t2}, the reactive current i_{rq2} is injected in proportion to the magnitude of U_{t2} [3]. In addition, the active current i_{rd2} should be limited by the capacity of converter $I_{\max}$

$$\begin{cases} i_{rq}2 = K_e(0.9 - U_{t2}) + i_{rq}1, s \\ 0 \le i_{rd}2 \le \sqrt{{I_{\max}}^2 - {i_{rq2}}^2} \end{cases} \tag{19}$$

where $i_{rq1,s}$ is the initial reactive current of stage 1, and K_e is the reactive current coefficient. As $1.5 \le K_e \le 3$ is often chosen in engineering, $K_e = 1.5$ is fixed in this article. $I_{\max} = 1.1$ p.u.. On the other hand, as U_{t2} in stage 2 only changes slightly, i_{rq2} in (19) is often chosen as fixed by the initial value of U_{t2} at stage 2. In a contrast, i_{rd2} can be treated as an adjustable parameter, subjected by the capacity constraint determined by i_{rq2} and $I_{\max}$.

Now the algebraic equations in (8) are unchanged, with the only one parameter change from U_{g1} ($U_{g1} = 1$ p.u.) to U_{g2}

$$\begin{cases} u_{td}2 = aU_{g2}\cos\varphi_{\text{pll}}2 - bX_g i_{rq}2 \\ u_{tq}2 = -cU_{g2}\sin\varphi_{\text{pll}}2 + dX_g i_{rd}2 \end{cases} \tag{20}$$

where the coefficients (a, b, c, and d) are all constants.

Considering the PLL's dynamics which is determined by $u_{tq}2$ only, and combining (19), (20), the DAEs accompanying with the capacity constraint are

$$\begin{cases} \dot{x}_{\text{pll}}2 = (k_{i\text{pll}}u_{tq}2)/\omega_0 \\ \dot{\varphi}_{\text{pll}}2 = \omega_0((k_{p\text{pll}}u_{tq}2)/\omega_0 + x_{\text{pll}}2 - 1) \end{cases} \tag{21}$$

$$\begin{cases} u_{tq}2 = -cU_{g2}\sin\varphi_{\text{pll}}2 + dX_g i_{rd}2 \\ 0 \le i_{rd}2 \le \sqrt{{I_{\max}}^2 - {i_{rq}2}^2}. \end{cases} \tag{22}$$

C. Stage 3: Early Postfault

When the fault is cleared and U_g recovers, U_{t3} is restored instantly and the TVC is unfrozen. Stage 3 starts. However, to protect device, the active power needs to recover gradually. In this stage, the linear recovery of i_{rd3} is constrained by the ramping rate K_{ramp}. The differential equations of the outer loop control in the MSC are

$$\begin{cases} \dot{i}_{rd3} = K_{\text{ramp}} \\ \dot{i}_{rq3} = k_{pV}\dot{U}_{t3} + k_{iV}(U_{t3} - {U_t}^*). \end{cases} \tag{23}$$

If the active power is restored too quickly, the electrical variables of the DFIG will oscillate violently and the unbalanced power on the shaft will be intensified, probably leading to torsional vibration. To suppress these effects, the ramping rate is generally set as relatively small [19], [23]. This might be different from the other renewable devices, such as the permanent magnet synchronous generator (PMSG) or photovoltaic (PV) systems. Oppositely, it also cannot be chosen too small, which might cause frequency issues. Therefore, $K_{\text{ramp}} > 0.2$ is often chosen in engineering [3]. In this article, $K_{\text{ramp}} = 0.8$ is selected.

Now with the major controls including the outer loop controls of the MSC and the PLL, the DAEs in stage 3 are

$$\begin{cases} \dot{i}_{rd3} = K_{\text{ramp}} \\ \dot{i}_{rq3} = k_{pV}\dot{U}_{t3} + k_{iV}(U_{t3} - {U_t}^*) \\ \dot{x}_{\text{pll}}3 = (k_{i\text{pll}}u_{tq}3)/\omega_0 \\ \dot{\varphi}_{\text{pll}}3 = \omega_0((k_{p\text{pll}}u_{tq}3)/\omega_0 + x_{\text{pll}}3 - 1) \end{cases} \tag{24}$$

$$\begin{cases} u_{td}3 = aU_{g3}\cos\varphi_{\text{pll}}3 - bX_g i_{rq}3 \\ u_{tq}3 = -cU_{g3}\sin\varphi_{\text{pll}}3 + dX_g i_{rd}3 \\ U_t 3 = \sqrt{{u_{td}3}^2 + {u_{tq}3}^2}. \end{cases} \tag{25}$$

D. Stage 4: Late Postfault

When the active current arrives at the initial level, i.e., $i_{rd3} = i_{rd1,s}$ in (17), the normal control is fully restored. Therefore, the model in stage 4 becomes exactly the same as that in stage 1.

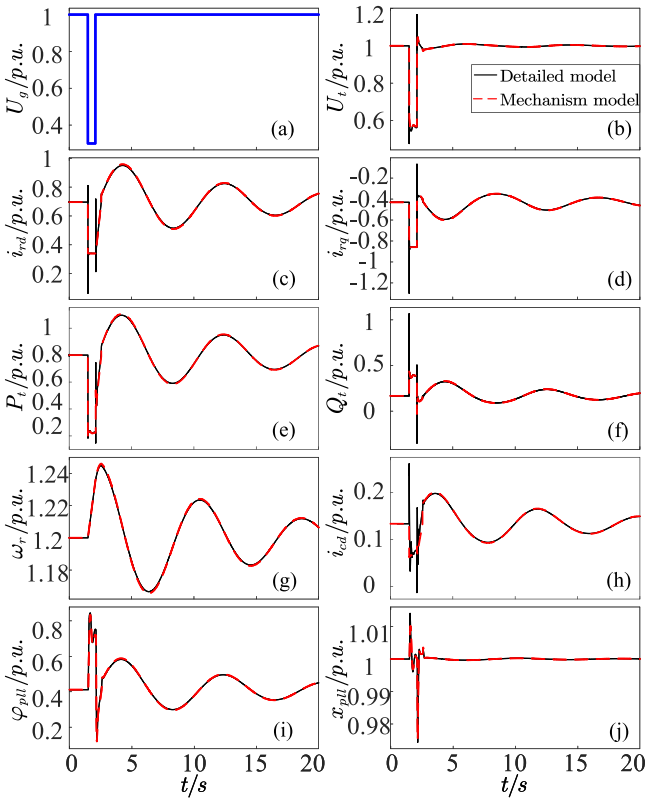

Fig. 6. (a)–(j) Plots of U_g, U_t, i_{rd}, i_{rq}, P_t, Q_t, ω_r, i_{cd}, φ_{pll}, and x_{pll}, respectively, for comparison of the mechanism model and the detailed model.

E. Simulation Verification and Summary

The above-mentioned mechanism model containing the whole four stages has been broadly verified in MATLAB/Simulink by comparison with the detailed model in Appendix B. As one example, at $t_f = 1.5$ s, U_g dips from 1 to 0.3 p.u.. At $t_c = 2.1$ s, the fault is cleared. The fault duration time $t_c - t_f = 0.6$ s. During the fault, $i_{rq2} = -0.86$ p.u. is calculated from (19) and $i_{rd2} = 0.34$ p.u. is chosen. The comparison results are shown in Fig. 6 and further in the magnified plots in Fig. 7, which displays the time-domain waveforms within the time window from 1 to 3 s. These results clearly indicate that the mechanism model is consistent with the detailed model, although some discernible fast dynamics at the switching moments of each stage are missed. In particular, some differences exist, regarding the fast dynamics of the GSC output current i_{cd} in Figs. 6(h) and 7(h), but the overall trend is consistent, which indicates that our assumption 3 is reasonable. In addition, in Figs. 6(g) and 7(g), ω_r fluctuates between 1.25 and 1.16 p.u., around 1.2 p.u. (the steady-state value). This indicates that the change of ω_r is tiny and it is reasonable to treat the two scales c and d in (22) as constants.

In summary, stage 1 provides an initial stable operating point. When a severe fault occurs and U_t drops below 0.8 p.u., the LVRT control is activated and stage 2 starts. Stage 2 (under U_{g2}) provides voltage support and the active-power current i_{rd2} can be regarded as an adjustable parameter. After the fault is cleared, U_t recovers instantly. Stage 3 (under U_{g3}) starts and

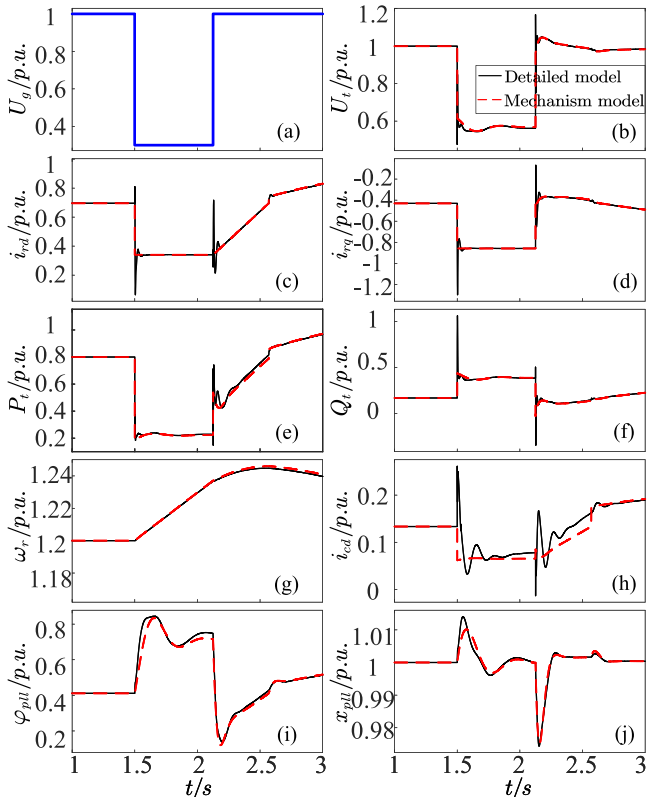

Fig. 7. (a)–(j) Magnified plots of Fig. 6 within 1–3 s.

i_{rd3} needs to recover gradually. When the i_{rd3} recovers to the initial level, stage 4 starts. Therefore, the whole LVRT processes of the DFIG system involve four stages, and basically the TSS should be determined by whether the final stage 4 can settle in a SEP of stage 4 [33]. Afterward, it will be very interesting to see that based on the dynamical characteristics of stage 3, this criterion can be greatly loosed and the TSS can become easier.

IV. TSS Analysis of Stage 2

There are many studies focusing on the TSS of stage 2 under the condition of permanent faults or using the concept of so-called device stability, which is much more power-electronics orient, but not power-system orient [13], [14], [15], [16]. Namely, only if the grid-tied device keeps synchronization on stage 2, the system can be stable, under the condition that the following stages 3 and 4 have been completely ignored. In addition, within this framework, the existence of SEP and small-signal stability of stage 2 have been widely investigated. It is necessary to start from this simple case first.

A. Generalized Swing Equation

According to the DAEs in stage 2 in (21) and (22), the following GSE with the pure ordinary differential equation can be derived

$$M_{\text{eq2}}\ddot{\varphi}_{\text{pll2}} = P_{m2} - P_{e2} - D_{\text{eq2}}\dot{\varphi}_{\text{pll2}} \tag{26}$$

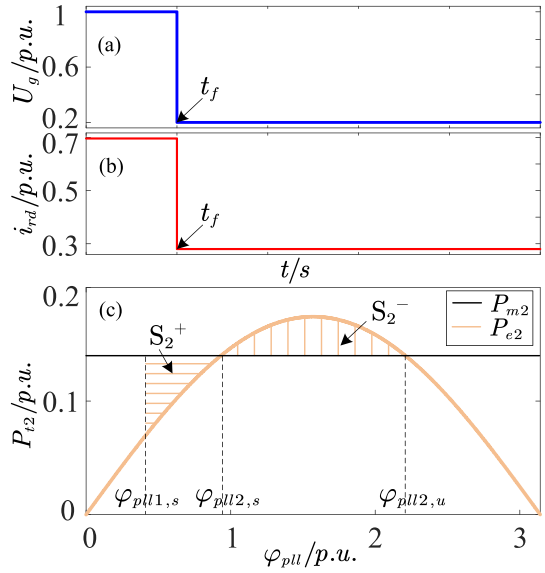

Fig. 8. (a) and (b) Plots of U_g and i_{rd}, and (c) EAC-based TSS analysis for permanent faults.

where

$$\begin{cases} P_{m2} = dX_g i_{rd2} \\ P_{e2} = cU_g 2\sin\varphi_{\text{pll2}} \\ M_{\text{eq2}} = \frac{1}{k_{\text{ipll}}} \\ D_{\text{eq2}} = c\frac{k_{\text{ppll}}}{k_{\text{ipll}}}U_{g2}\cos\varphi_{\text{pll2}} \end{cases} \tag{27}$$

where P_{m2}, P_{e2}, M_{eq2}, and D_{eq2} represent the equivalent mechanical power, electromagnetic power, inertia, and damping, respectively. Clearly, P_{m2} is a constant, depending on i_{rd2}, and P_{e2} is a sinusoidal function of φ_{pll2}, depending on U_{g2}. Different from that the PMSG and PV control the current of the GSC, the DFIG usually controls the current of the MSC to achieve LVRT. This difference gives rise to the correction coefficients c and d in the GSE.

B. EAC-Based TSS Assessment for Voltage-Dip Permanent Faults

After ignoring the damping term in the GSE, the EAC can be used to analyze the TSS in stage 2 for permanent faults, as shown in Fig. 8. Before the fault, the system is working at the initial operating point of stage 1, as shown in (17)

$$\varphi_{\text{pll1},s} = \arcsin\left(\frac{P_{\text{in}}X_g}{U_{g1}U_t^*}\right) = \arcsin\left(\frac{dX_g i_{rd1}}{cU_{g1}}\right). \tag{28}$$

The second equality comes from the second equation in (8) under the steady-state value $u_{tq}1,\text{s} = 0$.

Without losing generality, when U_g dips (e.g., U_g =0.2 p.u.) and a permanent fault occurs at t_f, stage 2 starts. $i_{rq2} = -0.93$ p.u. and $i_{rd2} = 0.28$ p.u. are chosen. The equivalent power angle (sinusoidal curve) P_{e2} and the equivalent constant mechanical power (horizontal line) P_{m2} are shown in Fig. 8(c). The SEP

and UEP of stage 2 are, respectively

$$\begin{cases} \varphi_{\text{pll}}2, s = \arcsin\left(\frac{dX_g i_{rd2}}{cU_{g2}}\right) \\ \varphi_{\text{pll}}2, u = \pi - \varphi_{\text{pll}}2, s. \end{cases} \tag{29}$$

The difference between $\varphi_{\text{pll}}2, s$ and $\varphi_{\text{pll}}1, s$ in (28) and (29) lies in the different values of U_g and i_{rd}. When a fault occurs, since $P_{m2} > P_{e2}$ at $\varphi_{\text{pll}1,s}$, $\varphi_{\text{pll}2}$ will accelerate. When $\varphi_{\text{pll}2,s} < \varphi_{\text{pll}2} < \varphi_{\text{pll}2,u}$, as $P_{m2} < P_{e2}$, $\varphi_{\text{pll}2}$ will decelerate. This happens until it arrives at $\varphi_{\text{pll}2,u}$. Therefore, the accelerating area ${S_2}^+$ and the maximal decelerating area ${S_2}^-$ are, respectively

$$\begin{cases} S_2^+ = \int_{\varphi_{\text{pll}1,s}}^{\varphi_{\text{pll}2,s}} (P_{m2} - P_{e2}) d\varphi_{\text{pll}2} \\ {S_2}^- = \int_{\varphi_{\text{pll}2,s}}^{\varphi_{\text{pll}2,u}} (P_{e2} - P_{m2}) d\varphi_{\text{pll}2}. \end{cases} \tag{30}$$

Based on the EAC, to ensure the TSS of stage 2 under the permanent faults, the following condition needs to meet:

$${S_2}^+ \le {S_2}^-. \tag{31}$$

According to (27), for a larger U_{g2}, P_{e2} becomes larger for a steeper curve, which is beneficial to the TSS. By a smaller i_{rd2}, P_{m2} decreases for a lower horizontal line, and the TSS can also be improved. All these are in accordance with our common sense. Next the TSS considering the whole LVRT process will be studied and the impact of stage 3 dynamics will be concentrated.

V. Transient Dynamical Analysis of Stage 3

A. Nonautonomous Driving-Response System

Observing the DAEs in stage 3 in (24) and (25) carefully, one can find that actually they can be divided into the following two subsystems including the driving one:

$$\begin{cases} \dot{x}_{\text{pll}3} = (k_{i\text{pll}} u_{tq3})/\omega_0 \\ \dot{\varphi}_{\text{pll}3} = \omega_0((k_{p\text{pll}} u_{tq3})/\omega_0 + x_{\text{pll}3} - 1) \end{cases} \tag{32}$$

$$\begin{cases} u_{tq}3 = -cU_{g3} \sin \varphi_{\text{pll}}3 + dX_g i_{rd3} \\ i_{rd3} = i_{rd2} + K_{\text{ramp}}(t - t_c) \end{cases} \tag{33}$$

and the other response one

$$\dot{i}_{rq3} = k_{pV} \dot{U}_{t3} + k_{iV}(U_{t3} - U_{\text{tref}}) \tag{34}$$

$$\begin{cases} u_{td}3 = aU_{g3} \cos \varphi_{\text{pll}}3 - bX_g i_{rq3} \\ U_t 3 = \sqrt{{u_{td}3}^2 + {u_{tq}3}^2}. \end{cases} \tag{35}$$

Clearly in the driving subsystem, u_{tq3} is affected by i_{rd3}, which depends on time. While for the response subsystem, u_{td3} is affected by $\varphi_{\text{pll}3}$ and i_{rq3}, and U_{t3} is affected by u_{tq3} which should come from the driving subsystem.

In the driving subsystem, as i_{rd3} increases linearly, it exhibits the nonautonomous characteristics. However, if its dynamics changes slowly, i_{rd3} can be approximately treated as a constant and hence the driving subsystem can be considered as a generalized autonomous system. Similar treatments have been widely used in the slow–fast nonautonomous analysis in mathematics [34]. Therefore, the dominant dynamics of stage 3 in (32) and (33) can be viewed as a series of PLL second-order dynamics

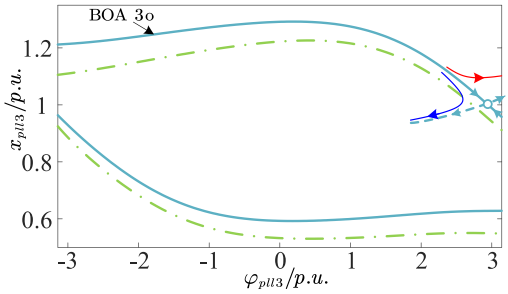

Fig. 9. Illustrations of different BOA boundaries under different values of $i_{rd}3$ and local dynamics near the UEP (open circle). The light blue solid (green dot-dashed) line represents the BOA at the initial (end) state of stage 3 for $i_{rd3} = i_{rd2} = 0.34$ p.u. ($i_{rd3} = i_{rd1,s} = 0.7$ p.u.).

in (21) and (22) [or in (26) and (27)] under an extremely slow change of i_{rd3} and a fixed U_{g3} (usually $U_{g3} > U_{g2}$). It is similar to the stage 2 dynamics essentially.

B. Dynamical Characteristics of Stage 3

With a constant i_{rd3}, it can be similarly studied on the $x_{\text{pll}} - \varphi_{\text{pll}}$ plane. The different BOA boundaries under different i_{rd3}'s are illustrated in Fig. 9. The light blue solid (green dot-dashed) line represents the BOA at the initial (end) state of stage 3 for $i_{rd3} = i_{rd2} = 0.34$ p.u. ($i_{rd3} = i_{rd1,s} = 0.7$ p.u.) Since the initial state of stage 3 under i_{rd2} and U_{g3} will be the most concerned, its BOA is emphasized by BOA 3o. Based on this comparison, it can be found that with a slow increase of i_{rd3}, the BOA moves to the lower left part slowly and the bulk structure of the BOA is unchanged.

On the other hand, it is well known that the local dynamics near the UEP represented by an open circle always dominates the TSS. If the system is within the BOA 3o and near the unstable manifold of the UEP, it will quickly move away from the UEP. The moving speed is usually much faster than that of the BOA. On the contrary, if the system is out of the BOA 3o and on the other side of the unstable manifold of the UEP, it will quickly move away from the UEP to the upper right direction.

Based on these two combined effects determined by the slow motion of the BOA and the local manifold structure near the UEP, it can easily derive that the initial state of stage 3 is dominant for the TSS, namely, if it is within the BOA 3o, the system will be stable, or otherwise, it will be unstable. Therefore, the following stages 3 and 4 after this particular initial moment of stage 3 do not need to be considered. However, fundamentally different from the TSS for the permanent faults in Section IV, here the LVRT effect is taken into account. All these analyses need to be verified by simulations.

C. Simulation Verification

Different cases have been widely studied. Without losing generality, three typical cases with the time domain simulation results of i_{rd} and φ_{pll} are shown in Fig. 10. The fault is set as U_g dips to 0.2 p.u. at $t_f = 0.5$ s, $i_{rq2} = -0.93$ p.u., with all other parameters in Appendix A. For the tests, three different values of i_{rd2} and t_c are chosen as follows.

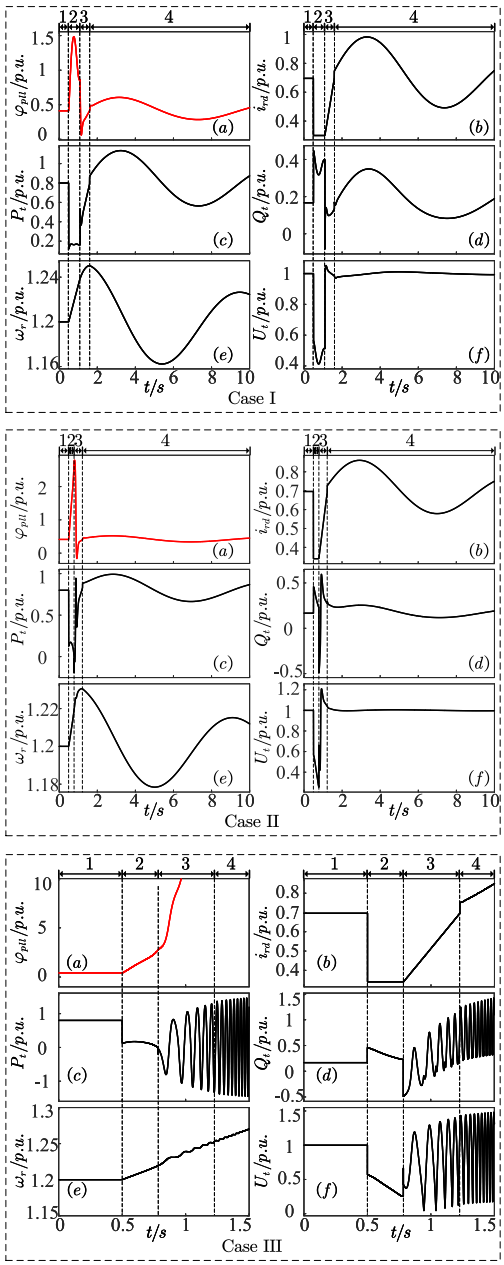

Fig. 10. Time domain simulation results of cases I, II, and III. Here, (a)–(f) represent the time-domain waveforms of φ_{pll}, i_{rd}, P_t, Q_t, ω_r, and U_t, respectively. Case I: i_{rd2} =0.3 p.u. and $t_c = 1.1$ s, case II: i_{rd2} =0.34 p.u. and $t_c = 0.782$ s, and and case III: i_{rd2} =0.34 p.u. and $t_c = 0.783$ s.

Case I: i_{rd2} =0.3 p.u., $t_c = 1.1$ s, and the fault duration time is $t_c - t_f = 0.6$ s.

Case II: i_{rd2} =0.34 p.u., $t_c = 0.782$ s, and $t_c - t_f = 0.282$ s.

Case III: i_{rd2} =0.34 p.u., $t_c = 0.783$ s, and $t_c - t_f = 0.283$ s.

Clearly in Fig. 10(a), the system is stable in stage 2 and finally keeps stable in stage 4. In a contrast, from the plot of φ_{pll} in Fig. 10(b), one can see that φ_{pll} keeps increasing, posing a risk of instability. However, due to a timely removal of the fault, the system eventually becomes stable in stage 4. If t_c is slightly larger, the system will eventually become unstable as shown in Fig. 10(c). When φ_{pll} continuously deviates, according

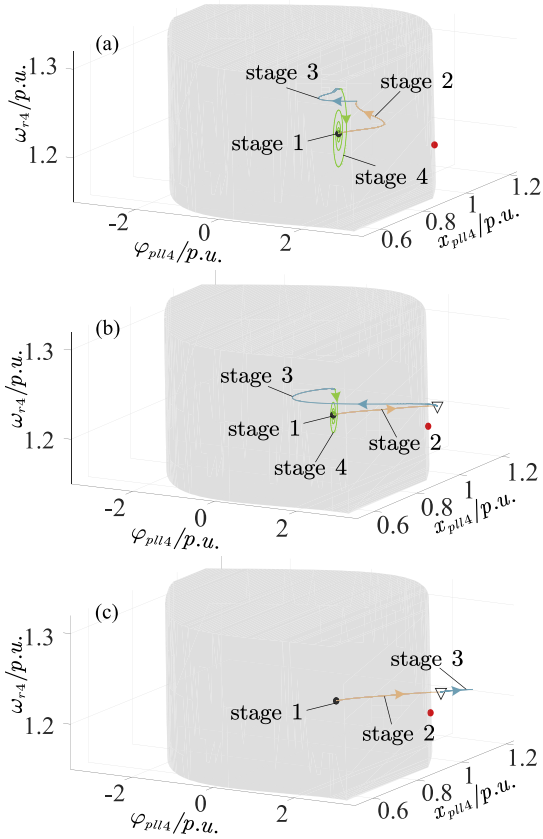

Fig. 11. (a)–(c) Comparisons of BOA in the ω_r-φ_{pll}-x_{pll} 3-D space in stage 4 and its fault trajectory for cases I, II, and III, respectively. A black hollow triangle for the initial state of stage 3 is superimposed in (b) and (c).

to (20), the terminal voltage will also oscillate with the phase deviation, and further affect the power to oscillate and give rise to instability. Eventually, the rotor speed will be affected by the continuous power imbalance and stall. These indicate that the phase of the φ_{pll} plays an important role in the transient stability of the system. Moreover, by comparing case II with case III in Fig. 10, it displays that even the system is unstable in stage 2, if the fault can be removed in time, the stability can still recover. Clearly these new findings imply that the previous EAC-based TSS assessment for permanent faults loses some important information, and the existence of an equilibrium point in stage 2 and the relevant TSS for the device stability in stage 2 are not necessary [27].

To show these three cases better, their BOA's in stage 4 and fault trajectories are shown in the ω_r-φ_{pll}-x_{pll} 3-D space and the φ_{pll}-x_{pll} 2-D plane in Figs. 11 and 12, respectively. As it is difficult to display the BOA in the full 5-D space, Fig. 11 is a projection, by the other two variables i_{rd} and i_{rq} fixed as $i_{rd1,u}$ and $i_{rq1,u}$ in (18). As shown in Figs. 11(a) and 12(a), if the trajectory is within the BOA of stage 2, then the system will be stable eventually. However, if an inappropriate active current is selected, instability will occur.

To emphasize the key difference in cases II and III induced by the different clearing-fault time t_c, a black hollow triangle for the initial state of stage 3 is superimposed correspondingly

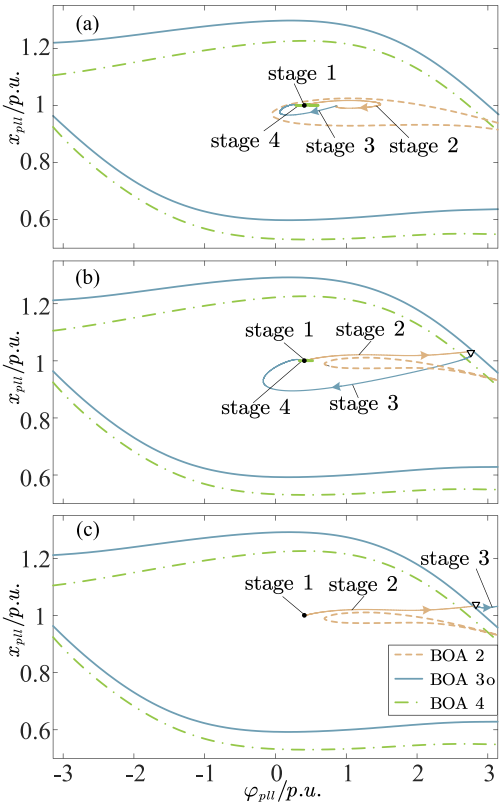

Fig. 12. Same as Fig. 11, but for comparisons on the φ_{pll}-x_{pll} 2-D plane, instead. Similarly, a black hollow triangle for the initial state of stage 3 is superimposed in (b) and (c). This clearly demonstrates that the relation between the initial state of stage 3 and the BOA 3o is dominant in the TSS. (a)–(c) Comparisons of BOA in the ω_r-φ_{pll}-x_{pll} 3-D space in stage 4 and its fault trajectory for cases I, II, and III, respectively. The orange dash line, the light blue solid line and the green dot-dashed line represent BOA 2, BOA 3o and BOA 4 respectively. The color of the trajectory in different stage also corresponds to it.

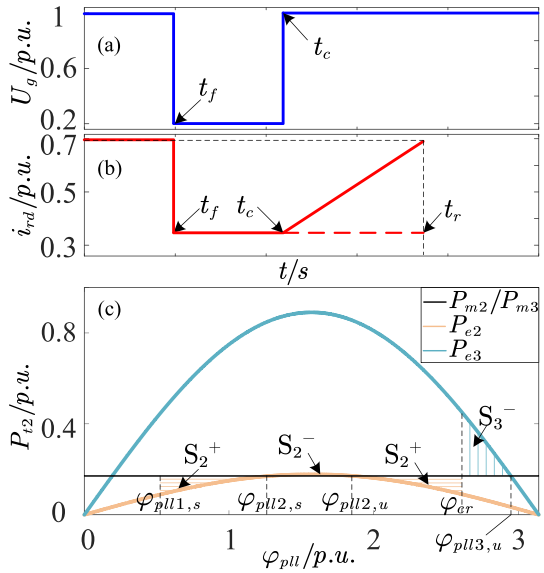

Fig. 13. Similar to Fig. 8, but for the TSS assessment considering the whole LVRT processes, instead, where the voltage recovery and the active current climbing are clear. Here the initial state of stage 3 is dominant and the actual active current climbing is unnecessary in the TSS analysis. For details, see the text. (a)–(c) Comparisons of BOA in the ω_r-φ_{pll}-x_{pll} 3-D space in stage 4 and its fault trajectory for cases I, II, and III, respectively. The orange dash line, the light blue solid line and the green dot-dashed line represent BOA 2, BOA 3o and BOA 4 respectively. The color of the trajectory in different stage also corresponds to it.

in Figs. 11 and 12(b)–(c). In addition, the boundaries of BOA 2 and BOA 3o are superimposed in Fig. 12 by dashed and solid curves, respectively. It clearly shows that in Fig. 12(b) and (c) the hollow triangle is outside the BOA of stage 4 in cases II and III, but it is inside of BOA 3o. In a contrast, in Fig. 12(c), it is outside of BOA 3o. Therefore, Fig. 12 clearly demonstrates that the relationship between the initial state of stage 3 and the BOA 3o truly plays a determinant role, namely, if it is within (out of) the BOA 3o, the system will be stable (unstable). The TSS can be determined immediately by the initial moment of stage 3. Consequently, with this BOA-based method, the TSS can be well predicted.

VI. Novel EAC-Based TSS Assessment Considering Whole LVRT Processes

A. Novel EAC-Based TSS Assessment

After catching the dominant factor in the TSS, it is necessary to extend the EAC-based assessment for the permanent faults in Section IV to the assessment considering the whole LVRT processes. Without losing generality, in Fig. 13(a), a severe fault occurs at t_f, U_g dips. The fault is cleared at t_c and U_g is restored. In addition, the variation of i_{rd2} is schematically shown by the solid lines in Fig. 13(b). In stage 3, i_{rd3} should linearly increases from i_{rd2} to i_{rd1}. As the system stability is solely determined by the relation between the initial state of stage 3 and the BOA 3o, for the TSS analysis, the system can be virtually viewed as staying at the stage 3 for ever, i.e., $i_{rd3} = i_{rd2}$ permanently, as shown the added dashed line in Fig. 13(b). In this respect, the only difference with the EAC analysis in Fig. 8 is that the U_g's recovery is incorporated.

In the EAC analysis in Fig. 13, now $P_{m3} = P_{m2}$, as the virtual value of i_{rd3} is fixed as $i_{rd3} = i_{rd2}$. The expression of the equivalent electromagnetic power P_{e2}/P_{e3} are shown in (27), with the only difference that U_g is different. Therefore, as $U_{g3} > U_{g2}$, $P_{e3} > P_{e2}$. These construct the basic relation between the equivalent mechanical and electromagnetic powers and their changes in the EAC analysis. Similarly, the UEP of stage 3 $\varphi_{\text{pll3},u}$ is important, and

$$\varphi_{pll3,u} = \pi - \arcsin\left(\frac{dX_g i_{rd3}}{cU_{g3}}\right). \tag{36}$$

Therefore, based on the EAC, the total accelerating area $S_{\Sigma 2}{}^+$ in stage 2 (starting at $\varphi_{\text{pll1},s}$ and ending at the critical clearing angle φ_{cr}) and the maximal decelerating area $S_3{}^-$ in stage 3 (starting at φ_{cr} and ending at $\varphi_{\text{pll3},u}$) are

$$\begin{cases} S_{\Sigma 2}^{+} = \int_{\varphi_{\text{pll1},s}}^{\varphi_{\text{cr}}} (\mathrm{P}_{m2} - \mathrm{P}_{e2}) \mathrm{d}\varphi_{\text{pll2}} \\ S_3{}^{-} = \int_{\varphi_{cr}}^{\varphi_{\text{pll3},u}} (P_{e3} - P_{m3}) d\varphi_{\text{pll3}}. \end{cases} \tag{37}$$

For the critical stability, $S_{\Sigma 2}{}^+ = S_3{}^-$. Correspondingly, the critical clearing angle φ_{cr} can be calculated by

$$\varphi_{cr} = \arccos\left(\frac{dX_g i_{rd2}(\varphi_{\text{pll3},u} - \varphi_{\text{pll1},s})}{c(U_{g3} - U_{g2})}\right.$$

TABLE I
COMPARISON OF CCT UNDER DIFFERENT VALUES OF U_{g2} AND i_{rd2}

U_{g2}/i_{rq2} (p.u.)	i_{rd2} (p.u.)	EMT	BOA-based		EAC-based	
		CCT	CCT	relative error	CCT	relative error
0.1/–1	0.3	0.157 s	0.158 s	+ 0.6%	0.143 s	- 8.9%
	0.4	0.114 s	0.115 s	+ 0.9%	0.099 s	-13.2%
0.2/–0.93	0.34	0.282 s	0.283 s	+ 0.4%	0.270 s	- 4.3%
	0.5	0.124 s	0.125 s	+ 0.8%	0.109 s	-12.2%
0.3/–0.86	0.5	0.252 s	0.253 s	+ 0.4%	0.239 s	- 5.2%
	0.6	0.140 s	0.141 s	+ 0.7%	0.125 s	-10.7%

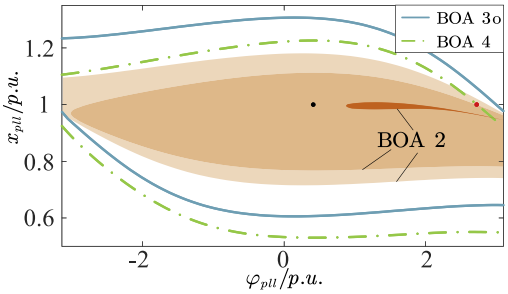

Fig. 14. BOA under different voltage drop depths U_{g2}. Among them, the orange area represents BOA 2, and the colors from light to dark correspond, respectively, to the BOA 2 under $U_{g2} = 0.55$ p.u., $U_{g2} = 0.35$ p.u., and $U_{g2} = 0.15$ p.u. The solid blue line represents BOA 3o, and the dotted green line represents BOA 4. The black dots represent the SEP in stage 1, and the red dots represent the UEP in stage 1.

$$+\frac{U_{g3}\cos\varphi_{\text{pll3},u} - U_{g2}\cos\varphi_{\text{pll1},s}}{U_{g3} - U_{g2}}\Bigg). \tag{38}$$

Next combining the numerical calculation of trajectory, the CCT can be obtained, similar to the TSS analysis in the traditional power systems.

The CCTs are calculated by the EMT simulation, BOA-based method, and EAC-based method under different values of U_{g2} and i_{rd2}. The results are shown in Table I. The relative errors of the two methods are compared with the EMT simulation. They show that in the BOA-based method the CCTs are always conservative and the relative error is very small, less than 1%. The reason might come from the BOA of stage 3 actually moves, depending on K_{ramp}, and is not completely stationary. In addition, the relative error of the EAC-based method is approximately within 13%, which is still acceptable, and its CCT is always radical. This might come from neglecting the damping term in the EAC.

B. Parameters Analysis

Based on the above-mentioned analysis, we have realized that the initial moment of stage 3 plays a very important role in the transient stability. Next, we will further analyze the influences of U_{g2}, i_{rd2}, and K_{ramp}.

1) Influence of U_{g2}: As shown in Fig. 14, the drop depth of the U_g only changes the size of BOA 2, without changing BOA 3o and BOA 4. The initial point of the system at the moment of a fault occurrence is fixed, as shown by the black point in Fig. 14. Therefore, U_{g2} mainly affects the final transient stability of the system by influencing the BOA 2.

As the U_{g2} decreases, BOA 2 will continue to shrink. This is very easy to understand. As shown in Fig. 13, when U_{g2} decreases, P_{e2} in stage 2 will correspondingly decrease, thus causing the decelerating area to continuously shrink and deteriorate stability. In the extreme cases, the operating point will be lost, and then a loss of synchronization will occur [9].

For instance, in Fig. 14, when $U_{g2} = 0.55$ p.u., since the initial point is within BOA 2, the phase φ_{pll} will converge near the operating point of stage 2. However, when $U_{g2} = 0.15$ p.u., at the beginning of stage 2, the initial point will fall outside of BOA 2. In this case, the phase φ_{pll} will increase rapidly and transient instability will occur in stage 2. Nevertheless, as long as the fault is cleared in time, transient stability can be maintained in the final stage.

To verify this point, we set up three groups of simulations, as shown in Fig. 15. In cases I, II, and III, the same parameters are adopted: $i_{rd2} = 0.25$ p.u., $K_{\text{ramp}} = 0.8$ p.u.. The fault occurred at $t_f = 0.5$ s. The differences lie in the magnitude of U_{g2} and the time of fault clearance t_c. Case I: $U_{g2} = 0.55$ p.u., $t_c = 1.125$ s; case II: $U_{g2} = 0.35$ p.u., $t_c = 1.125$ s; case III: $U_{g2} = 0.15$ p.u., $t_c = 0.853$ s. As shown in Fig. 15, the reduction of U_{g2} truly increases the risk of transient instability.

2) Influence of i_{rd2}: As shown in Fig. 16, the magnitude of i_{rd2} simultaneously alters the sizes of BOA 2 and BOA 3o, but does not affect BOA 4. The initial point of the system at the time of the fault is fixed, which is provided by stage 1, as indicated by the black dot in Fig. 16.

As in Fig. 13, when i_{rd2} increases, the equivalent mechanical power of the stage 2 (P_{m2}) and the initial moment of stage 3 (P_{m3}) will increase accordingly, which leads to a reduction in the decelerating region and a deterioration in stability. For instance, in Fig. 16, when $i_{rd2} = 0.1$ p.u., both BOA 2 and BOA 3o are large, ensuring stability at the stage 2 and the initial moment of stage 3. However, when $i_{rd2} = 0.5$ p.u., at the initial moment of stage 2, the black point will fall outside BOA 2. In this case, the phase φ_{pll} will increase rapidly, and transient instability will occur in stage 2. In addition, BOA 3o shrinks and moves to the left, and its trajectory will meet earlier, which means the transient stability margin of the system deteriorates. Therefore, this requires a shorter time to clear the fault.

To verify this point, we set up three groups of simulations, as shown in Fig. 17. In cases I, II, and III, the same parameters are adopted: $U_{g2} = 0.3$ p.u., $K_{\text{ramp}} = 0.8$ p.u.. The fault occurs at $t_f = 0.5$ s. The differences lie in the magnitude of i_{rd2} and the time of fault clearance t_c. Case I: $i_{rd2} = 0.1$ p.u., $t_c = 1.125$ s; case II: $i_{rd2} = 0.3$ p.u., $t_c = 1.125$ s; case III: $i_{rd2} = 0.5$ p.u., $t_c = 0.725$ s. As shown in Fig. 17, the increase of i_{rd2} will increase the risk of transient instability. During the complete LVRT processes, an excessively low active power output can cause a significant energy deficit for the system, affecting the system's frequency stability. However, wind farms always aim to deliver as much active power as possible. Therefore, during fault, if wind turbines are required to maintain a certain level of active power output, they must sacrifice the corresponding transient stability margin. Fig. 16 provides a clear physical picture to understand the impact mechanism of increased active power output from wind turbines on the system's transient stability.

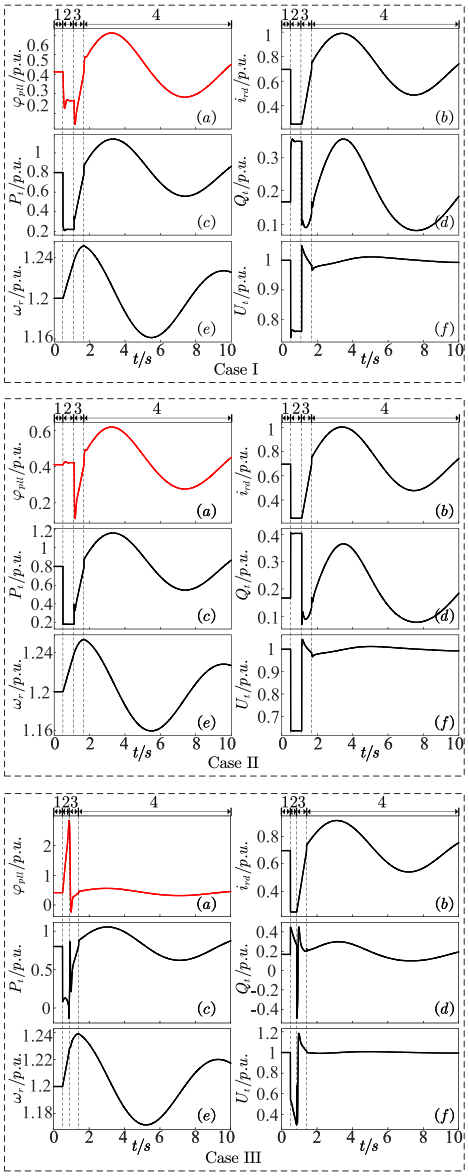

Fig. 15. Time-domain simulation under different voltage drop depths U_{g2}. Here, (a)–(f) represent the time-domain waveforms of φ_{pll}, i_{rd}, P_t, Q_t, ω_r, and U_t, respectively. Case I: $U_{g2} = 0.55$ p.u., case II: $U_{g2} = 0.35$ p.u., and case III: $U_{g2} = 0.15$ p.u.

3) Influence of K_{ramp}: The ramping rate K_{ramp} does not change the shape of the BOA, but only alters the movement speed of BOA in stage 3. Further to demonstrate the influence of K_{ramp}, the CCTs with different K_{ramp}'s under different methods are studied. $U_{g2} = 0.2$ p.u. and $i_{rd2} = 0.34$ p.u.. The results are shown in Table II. The CCT calculated by the BOA-based method is 0.283 s, and that calculated by the EAC-based method is 0.270 s. As these two methods are based on the initial moment of stage 3, their CCTs are not influenced by K_{ramp}. It can be found that as K_{ramp} increases, the CCT of the EMT result only slightly decreases. This is easy to understand: as the BOA moves faster, less time is required to clear faults. In addition, for a larger K_{ramp}, the relative error of the BOA-based method increases and oppositely that of the EAC-based method decreases. Nevertheless, the influence of K_{ramp} is tiny.

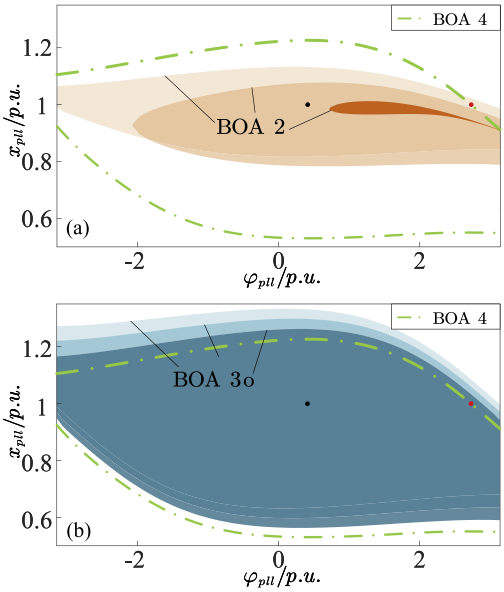

Fig. 16. BOA under different i_{rd2}'s. In (a), the orange area represents BOA 2, and the colors from light to dark correspond to the BOA 2 under $i_{rd2} = 0.1$ p.u., $i_{rd2} = 0.3$ p.u., and $i_{rd2} = 0.5$ p.u., respectively. In (b), the blue area represents BOA 3o, and the colors from light to dark correspond to the BOA 3o under $i_{rd2} = 0.1$ p.u., $i_{rd2} = 0.3$ p.u., and $i_{rd2} = 0.5$ p.u., respectively. The dotted green line represents BOA 4. The black dots represent the SEP in stage 1, and the red dots represent the UEP in stage 1.

TABLE II
COMPARISON OF CCT UNDER DIFFERENT K_{RAMP}'S

K_{ramp}	EMT	BOA-based	EAC-based
	CCT	relative error (CCT=0.283 s)	relative error (CCT=0.270 s)
0.2–1.1	0.282 s	+ 0.4%	- 4.3%
1.2–3.2	0.281 s	+ 0.7%	- 3.9%
3.3–5.3	0.280 s	+ 1.1%	- 3.6%
5.4–7.5	0.279 s	+ 1.4%	- 3.2%
7.6–9.9	0.278 s	+ 1.8%	- 2.9%

To verify this point, we set up three groups of simulations. The results are shown in Fig. 18. In cases I, II, and III, the same parameters are adopted: $U_{g2} = 0.2$ p.u., $i_{rd2} = 0.34$ p.u. The fault occurs at $t_f = 0.5$ s. The differences lie in the magnitude of K_{ramp}. Case I: $K_{\text{ramp}} = 0.8$ p.u.; case II: $K_{\text{ramp}} = 4.8$ p.u.; case III: $K_{\text{ramp}} = 8.8$ p.u. We can see that K_{ramp} has a little influence on CCT.

VII. EXPERIMENTAL VERIFICATION

In order to verify the above-mentioned analysis, hardware-in-the-loop experiments are conducted based on the SpaceR. The SpaceR real-time simulation platform is a system that integrates functions, such as real-time simulation, control, testing, rapid control prototyping, and hardware-in-the-loop testing. As shown in Fig. 19, the SpaceR real-time simulation platform consists of the host computer system, digital signal processing, oscilloscope, and SpaceR. It can simulate the dynamic behavior of the target model, and enable the integrated operation of

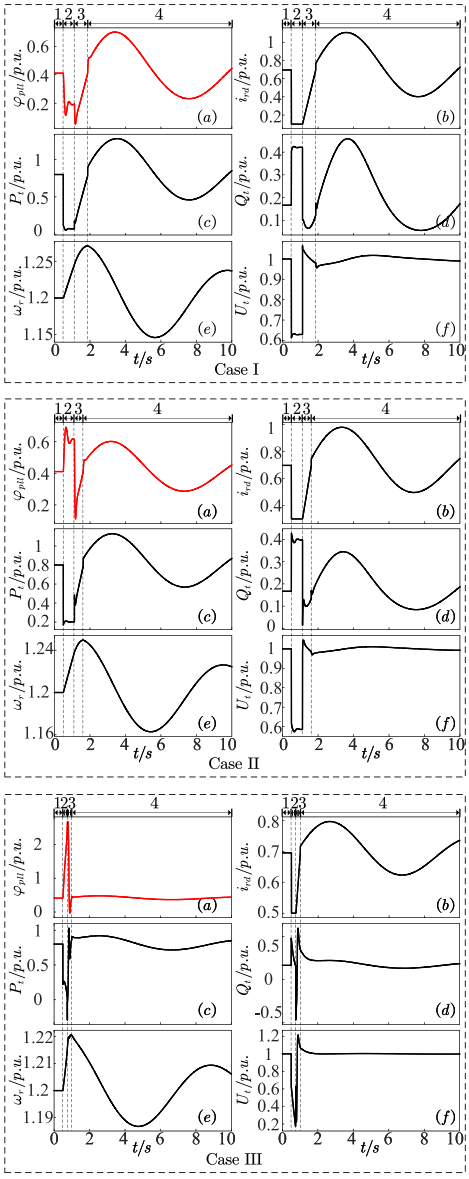

Fig. 17. Time-domain simulation under different i_{rd2}'s. Here, (a)–(f) represent the time-domain waveforms of φ_{pll}, i_{rd}, P_t, Q_t, ω_r, and U_t respectively. Case I: $i_{rd2} = 0.1$ p.u., case II: $i_{rd2} = 0.3$ p.u., and case III: $i_{rd2} = 0.5$ p.u.

the object model with the physical control system via digital signal processing equipment on the simulation platform, thereby facilitating the testing of the physical control system. The system model and most of the control parameters tested in the experiment are the same as in Fig. 1 and Appendix A. Here, four sets of experiments will be presented to verify the correctness of the above-mentioned mechanism analysis and stability assessment.

Case A: When $t_f = 5$ s, U_g dips to 0.2 p.u. At $t_c = 5.6$ s, U_g recovers to 1 p.u. The experimental results for $i_{rd2} = 0.1$, 0.3, and 0.4 p.u. are shown in Fig. 20(a)–(c), respectively. With increasing of i_{rd2}, the risk of transient instability increases. In Fig. 20(a) and (b), when the system is stable in stage 2, it can be stable finally. In Fig. 20(c), when the system is unstable in stage

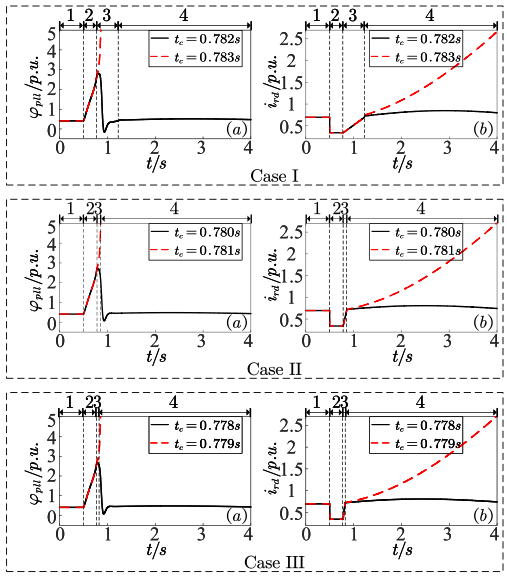

Fig. 18. Time-domain simulation under different K_{ramp}'s. Here, (a) and (b) represent the time-domain waveforms of φ_{pll} and i_{rd}, respectively. Case I: $K_{\text{ramp}} = 0.8$ p.u.; case II: $K_{\text{ramp}} = 4.8$ p.u., and case III: $K_{\text{ramp}} = 8.8$ p.u.

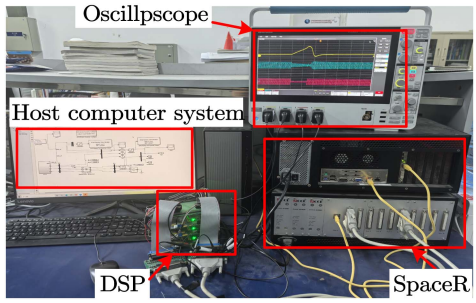

Fig. 19. SpaceR real-time simulation platform.

2, if the fault persists for a longer period of time, the system will eventually lose stability.

Case B: When $t_f = 5$ s, U_g dips to 0.1 p.u., $i_{rd2} = 0.3$ p.u. and $i_{rq2} = -1$ p.u. At t_c, U_g recovers to 1 p.u. The experimental results for two different fault clearing times $t_c = 5.159$ and 5.160 s are shown in Fig. 21(a) and (b), respectively. It is clear that with a slightly larger t_c in Fig. 21, although φ_{pll} is unstable in stage 2, the system can finally become unstable. Under this situation, the CCT is 0.159 s, well in accord with the EMT result: CCT = 0.157 s in Table I. These experimental results demonstrate that even if the system experiences transient instability in stage 2, as long as the fault is cleared in time, the system can ultimately be stable.

Case C: When $t_f = 5$s, U_g dips to 0.2 p.u., $i_{rd2} = 0.34$ p.u. and $i_{rq2} = -0.93$ p.u. At t_c, U_g recovers to 1 p.u. The experimental results for two different fault clearing times $t_c = 5.284$ and 5.285 s are shown in Fig. 22(a) and (b), respectively. Under this situation, the CCT is 0.284 s, well in accord with the EMT result: CCT = 0.282 s in Table I.

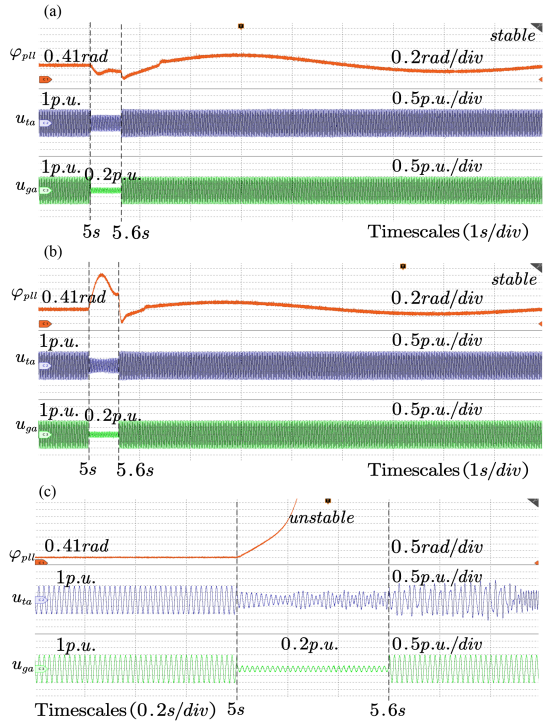

Fig. 20. (a)–(c) Experimental waveform diagrams of case A.

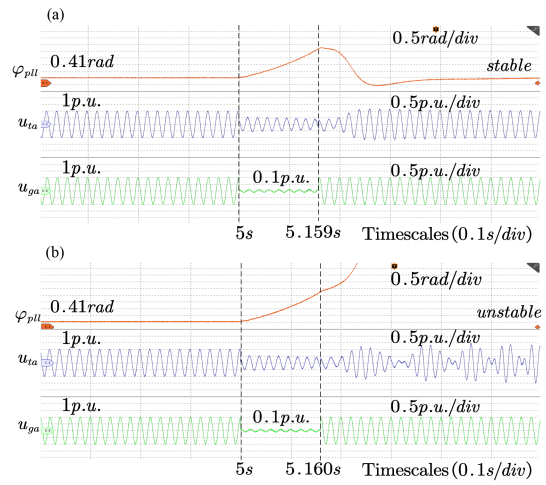

Fig. 21. (a) and (b) Experimental waveform diagrams of case B.

Case D: When $t_f = 5$ s, U_g dips to 0.3 p.u., $i_{rd2} = 0.5$ p.u. and $i_{rq2} = -0.86$ p.u. At t_c, U_g recovers to 1 p.u. The experimental results for two different fault clearing times $t_c = 5.255$ and 5.256 s are shown in Fig. 23(a) and (b), respectively. Under this situation, the CCT is 0.255 s, well in accord with the EMT result: CCT = 0.252 s in Table I. Therefore, cases B, C, and D all verify the effectiveness of the aforementioned stability assessment method and prove the correctness of the stability mechanism analysis.

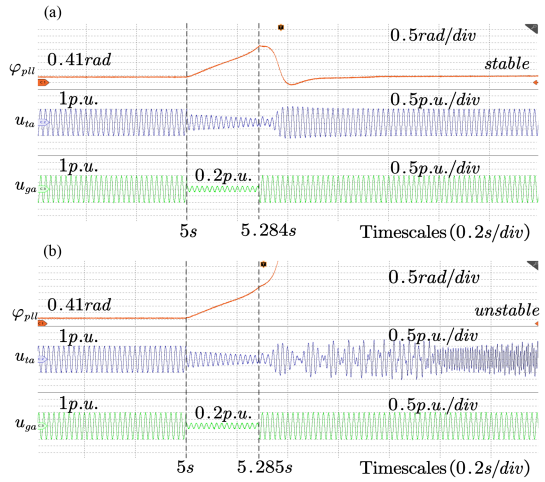

Fig. 22. (a) and (b) Experimental waveform diagrams of case C.

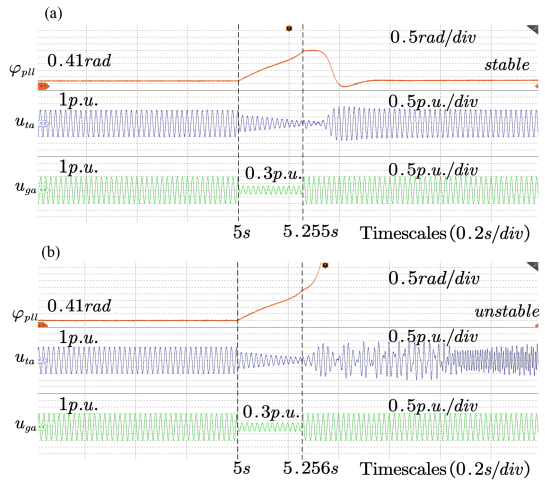

Fig. 23. (a) and (b) Experimental waveform diagrams of case D.

VIII. Conclusion

In conclusion, the TSS model, analysis, and assessment of the DFIG system considering complete LVRT processes have been systematically studied. The valuable conclusions are as follows.

1) According to the general sequential switching scheme of the LVRT, a transient mechanism model considering the complete LVRT processes is constructed. The dominant dynamical behaviors, switching conditions, and chief factors of each stage are studied in detail. Clearly the PLL dynamics is dominant and the GSE is important. The synchronization of DFIG with the grid as a whole can be well characterized by the dynamical behavior of the PLL output angle, which plays a similar role with rotor angle of SG.
2) By the salient property of the driving-response nonautonomous system of stage 3, the initial moment of stage 3 plays a decisive role in the TSS, namely, if the state is within (out of) the BOA 3o, it will remain within (out of)

the BOA 3 and the system will finally be stable (unstable). This greatly helps simplify the TSS analysis.

3) Standing on the dynamical characteristics of stages 2 and 3, two new TSS assessment methods, including the BOA-based and the EAC-based methods, are developed and compared. Their accuracy has been well verified by wide simulations and hardware-in-the-loop experiments. For most of cases, the error of the BOA-based method is within about only 1%, and that of the EAC-based method is within about 13%. Both are acceptable in engineering.
4) The present works not only provide a clear physical picture of the DFIG system with the LVRT and two efficient assessment methods for the TSS, but also exhibit guidance for enhancing transient synchronization stability.

APPENDIX

A Parameters Used in this Article

Parameters of grid: $S_{\text{base}} = 2$ MW, $U_{\text{base}} = 690$ V (line rms value), $U_{\text{dcbase}} = 1400$ V, $f_0 = 50$ Hz, $\omega_0 = 2\pi f_0$, ${U_{\text{dc}}}^* = 1$ p.u., ${U_t}^* = 1$ p.u., $U_g = 1$ p.u., $P_{\text{in}} = 0.8$ p.u., ${\omega_r}^* = 1.2$ p.u., $C = 0.05$ p.u., $L_f = 0.1$ p.u., $L_g = 0.5$ p.u.

Parameters of DFIG: $L_{Is} = 0.171$ p.u., $L_{Ir} = 0.156$ p.u., $L_m = 3.9$ p.u., $H = 4$ p.u.

Parameters of controller: 1) RSC: $k_{pw} = 1$, $k_{iw} = 5$. 2) TVC: $k_{pV} = 1$, $k_{iV} = 10$. 3) PLL: $k_{\text{ppll}} = 60$, $k_{\text{ipll}} = 1400$. 4) DVC: $k_{pudc} = 1.5$, $k_{iudc} = 160$. 5) ACC: $k_{purd} = 0.6$, $k_{iurd} = 80$, $k_{purq} = 0.6$, $k_{iurq} = 80$, $k_{pucd} = 4$, $k_{iucd} = 300$, $k_{pucq} = 4$, $k_{iucq} = 300$. 6) LVRT: $K_e = 1.5$. 7) Ramp: $K_{\text{ramp}} = 0.8$.

B Detailed Model of DFIG System

The detailed model of the DFIG system of stage 1 will be introduced. The models of other stages will be obtained similarly.

1) Dynamics of the Asynchronous Machine: The asynchronous machine mainly consists of two parts. The rotor dynamics is

$$\dot{\omega}_{r1} = \frac{P_{\text{in}} - P_{t1}}{2H\omega_{r1}} \tag{B.1}$$

and the flux linkage dynamics are

$$\begin{cases} \dot{\psi}_{rd1} = \omega_0 \left(u_{rd1} - R_r i_{rd1} + s_p \psi_{rq1}\right) \\ \dot{\psi}_{rq1} = \omega_0 \left(u_{rq1} - R_r i_{rq1} - s_p \psi_{rd1}\right) \\ \dot{\psi}_{sd1} = \omega_0 \left(u_{td1} + R_s i_{sd1} - \omega_g \psi_{sq1}\right) \\ \dot{\psi}_{sq1} = \omega_0 \left(u_{tq1} + R_s i_{sd1} + \omega_g \psi_{sd1}\right) \end{cases} \tag{B.2}$$

$$\begin{cases} \psi_{rd1} = X_r i_{rd1} - X_m i_{sd1} \\ \psi_{rq1} = X_r i_{rq1} - X_m i_{sq1} \\ \psi_{sd1} = X_m i_{rd1} - X_s i_{sd1} \\ \psi_{sq1} = X_m i_{rq1} - X_s i_{sq1} \end{cases} \tag{B.3}$$

where X_s, X_r, and X_m are the per-unit values of stator reactance, rotor reactance, and mutual inductance reactance, respectively. R_s and R_r are the per-unit values of stator resistance and rotor resistance, respectively. In actual analysis, since the resistances are very small, they are ignored. ω_g is the per-unit value of grid-side frequency, which is approximately considered as $\omega_g \approx 1$. ω_0 is the reference value of frequency (100π rad/s), and $s_p = (\omega_g - \omega_r)/\omega_g$ is the slip ratio.

By transforming (B.3), the expressions of the stator and rotor currents can be obtained

$$\begin{cases} i_{rd1} = \left(X_m \psi_{sd1} - X_s \psi_{rd1}\right) / \left({X_m}^2 - X_r X_s\right) \\ i_{rq1} = \left(X_m \psi_{sq1} - X_s \psi_{rq1}\right) / \left({X_m}^2 - X_r X_s\right) \\ i_{sd1} = \left(X_r \psi_{sd1} - X_m \psi_{rd1}\right) / \left({X_m}^2 - X_r X_s\right) \\ i_{sq1} = \left(X_r \psi_{sq1} - X_m \psi_{rq1}\right) / \left({X_m}^2 - X_r X_s\right). \end{cases} \tag{B.4}$$

2) Dynamics of the MSC: For the MSC, the dynamics of the outer-loop (RSC and TVC) are

$$\begin{cases} \dot{i}^*_{rd1} = k_{pw} \dot{\omega}_{r1} + k_{iw} \left(\omega_{r1} - {\omega_r}^*\right) \\ \dot{i}^*_{rq1} = k_{pV} \dot{U}_{t1} + k_{iV} \left(U_{t1} - {U_t}^*\right) \end{cases} \tag{B.5}$$

where k_{pw} and k_{iw} are the proportional and integral coefficients of the RSC, respectively, k_{pV} and k_{iV} are the proportional and integral coefficients of the TVC, respectively.

And the dynamics of the ac current control are

$$\begin{cases} \dot{u}_{rd1} = k_{purd} \left(\dot{i}^*_{rd1} - \dot{i}_{rd1}\right) + k_{iurd} \left(i^*_{rd1} - i_{rd1}\right) \\ \dot{u}_{rq1} = k_{purq} \left(\dot{i}^*_{rq1} - \dot{i}_{rq1}\right) + k_{iurq} \left(i^*_{rq1} - i_{rq1}\right) \end{cases} \tag{B.6}$$

where k_{purd} and k_{iurd} are, respectively, the proportional coefficient and integral coefficient of the d-axis ac current control, and k_{purq} and k_{iurq} are, respectively, the proportional coefficient and integral coefficient of the q-axis ac current control.

3) Dynamics of the GSC: For the GSC, the dynamics of the DVC is

$$\dot{i}^*_{cd1} = k_{pdc} \dot{u}_{dc1} + k_{idc} \left(u_{dc1} - u^*_{dc}\right) \tag{B.7}$$

where k_{pdc} and k_{idc} are, respectively, the proportional coefficient and integral coefficient of the DVC. Usually i^*_{cq1} is set to 0, i.e., $i^*_{cq1} = 0$.

And the dynamics of the ac current control are

$$\begin{cases} \dot{u}_{cd1} = k_{pucd} \left(\dot{i}^*_{cd1} - \dot{i}_{cd1}\right) + k_{iucd} \left(i^*_{cd1} - i_{cd1}\right) \\ \dot{u}_{cq1} = k_{pucq} \left(0 - \dot{i}_{cq1}\right) + k_{iucq} \left(0 - i_{cq1}\right) \end{cases} \tag{B.8}$$

where k_{pucd} and k_{iucd} are, respectively, the proportional coefficient and integral coefficient of the d-axis ac current control, and k_{pucq} and k_{iucq} are, respectively, the proportional coefficient and integral coefficient of the q-axis ac current control.

4) Dynamics of the PLL: The dynamics of the PLL are

$$\begin{cases} \dot{x}_{\text{pll1}} = \left(k_{i\text{pll}} u_{tq1}\right)/\omega_0 \\ \dot{\varphi}_{\text{pll1}} = \omega_0 \left(\left(k_{\text{ppll}} u_{tq1}\right)/\omega_0 + x_{\text{pll1}} - 1\right) \end{cases} \tag{B.9}$$

where k_{ppll} and $k_{i\text{pll}}$ are the proportional and integral coefficients of the PLL, respectively.

5) Dynamics of Filter Inductance L_f: The dynamics of the filter inductance L_f are

$$\begin{cases} \dot{i}_{cd1} = \omega_0 \left(u_{cd1} - u_{td1} + i_{cq1} X_f\right) / X_f \\ \dot{i}_{cq1} = \omega_0 \left(u_{cq1} - u_{tq1} - i_{cd1} X_f\right) / X_f \end{cases} \tag{B.10}$$

where X_f represents the per-unit value of the filter reactance.

6) Dynamics of the Dc Capacitor: The dynamics of the dc capacitor is

$$\dot{u}_{\mathrm{dc1}} = \frac{P_{r1} - P_{c1}}{2Cu_{\mathrm{dc1}}} \tag{B.11}$$

where C represents the per-unit value of the dc capacitor, P_{r1} and P_{c1} represent the active powers flowing through the MSC and the GSC, respectively, i.e.,

$$\begin{cases} P_{r1} = -u_{rd1}i_{rd1} - u_{rq1}i_{rq1} \\ P_{c1} = u_{cd1}i_{cd1} + u_{cq1}i_{cq1}. \end{cases} \tag{B.12}$$

7) Dynamics of Transmission Line L_g: The dynamics of the transmission line L_g are

$$\begin{cases} \dot{i}_{td1} = \omega_0 \left(u_{td1} - U_{g1}\cos\varphi_{\mathrm{pll1}} + i_{tq1}X_g\right)/X_g \\ \dot{i}_{tq1} = \omega_0 \left(u_{tq1} + U_{g1}\sin\varphi_{\mathrm{pll1}} - i_{td1}X_g\right)/X_g \end{cases} \tag{B.13}$$

where X_g represents the per-unit value of the transmission line reactance.

According to Kirchhoff's current law, it can be known that the total current on the grid line are

$$\begin{cases} i_{td1} = i_{sd1} + i_{cd1} \\ i_{tq1} = i_{sq1} + i_{cq1} \end{cases} \tag{B.14}$$

where i_{cd1} and i_{cq1} are known state variables, and the i_{sd1} and i_{sq1} can be obtained based on the state variables of magnetic flux linkage in (B.4). Therefore, the total line current i_{td1} and i_{tq1} will be able to be expressed by the existing state variables. Thus, (B.13) can be converted into it as follows:

$$\begin{cases} u_{td1} = \dot{i}_{td1}X_g/\omega_0 + U_{g1}\cos\varphi_{\mathrm{pll1}} - i_{tq1}X_g \\ u_{tq1} = \dot{i}_{tq1}X_g/\omega_0 - U_{g1}\sin\varphi_{\mathrm{pll1}} + i_{td1}X_g. \end{cases} \tag{B.15}$$

Combing (B.2), (B.4), (B.10), (B.14), and (B.15), we will obtain the explicit algebraic expressions of u_{td1} and u_{tq1}, by using the existing state variables

$$\begin{cases} u_{td1} = (\alpha_\psi + \alpha_f + U_{g1}\cos\varphi_{\mathrm{pll1}} - i_{tq1}X_g)/\eta_\Sigma \\ u_{tq1} = (\beta_\psi + \beta_f - U_{g1}\sin\varphi_{\mathrm{pll1}} + i_{td1}X_g)/\eta_\Sigma \end{cases} \tag{B.16}$$

here, the expressions of η_Σ, $\alpha_{\psi 1}$, $\beta_{\psi 1}$, α_{f1}, and β_{f1} are

$$\begin{cases} \eta_\Sigma = 1 + 1/X_f - X_rX_g/\left({X_m}^2 - X_rX_s\right) \\ \alpha_{\psi 1} = \dfrac{\begin{pmatrix} X_gX_r\left(R_si_{sd1} - \omega_g\psi_{sq1}\right) \\ -X_gX_m\left(u_{rd1} - R_ri_{rd1} + s_p\psi_{rq1}\right) \end{pmatrix}}{{X_m}^2 - X_rX_s} \\ \beta_{\psi 1} = \dfrac{\begin{pmatrix} X_gX_r\left(R_si_{sd1} + \omega_g\psi_{sd1}\right) \\ -X_gX_m\left(u_{rq1} - R_ri_{rq1} - s_p\psi_{rd1}\right) \end{pmatrix}}{{X_m}^2 - X_rX_s} \\ \alpha_{f1} = \left(u_{cd1} + i_{cq1}X_f\right)/X_f \\ \beta_{f1} = \left(u_{cq1} - i_{cd1}X_f\right)/X_f. \end{cases} \tag{B.17}$$

Furthermore, the total output power of DFIG and the amplitude of terminal voltage are

$$\begin{cases} P_{t1} = u_{td}1i_{td}1 + u_{tq}1i_{tq}1 \\ U_t1 = \sqrt{{u_{td1}}^2 + {u_{tq1}}^2}. \end{cases} \tag{B.18}$$

8) DAEs of Detailed Full-Order Model of DFIG System at Each Stage: In stage 1, combining (B.1), (B.2), (B.5)–(B.11), the differential equations of the detailed model of the DFIG system are as follows:

$$\begin{cases} \dot{\omega}_{r1} = (P_{\mathrm{in}} - P_{t1})/(2H\omega_{r1}) \\ \dot{\psi}_{rd1} = \omega_0\left(u_{rd1} - R_ri_{rd1} + s_p\psi_{rq1}\right) \\ \dot{\psi}_{rq1} = \omega_0\left(u_{rq1} - R_ri_{rq1} - s_p\psi_{rd1}\right) \\ \dot{\psi}_{sd1} = \omega_0\left(u_{td1} + R_si_{sd1} - \omega_g\psi_{sq1}\right) \\ \dot{\psi}_{sq1} = \omega_0\left(u_{tq1} + R_si_{sd1} + \omega_g\psi_{sd1}\right) \\ \dot{i}^*_{rd1} = k_{pw}\dot{\omega}_{r1} + k_{iw}\left(\omega_{r1} - {\omega_r}^*\right) \\ \dot{i}^*_{rq1} = k_{pV}\dot{U}_{t1} + k_{iV}\left(U_{t1} - {U_t}^*\right) \\ \dot{u}_{rd1} = k_{purd}\left(\dot{i}^*_{rd1} - \dot{i}_{rd1}\right) + k_{iurd}\left(i^*_{rd1} - i_{rd1}\right) \\ \dot{u}_{rq1} = k_{purq}\left(\dot{i}^*_{rq1} - \dot{i}_{rq1}\right) + k_{iurq}\left(i^*_{rq1} - i_{rq1}\right) \\ \dot{i}^*_{cd1} = k_{pdc}\dot{u}_{dc1} + k_{idc}\left(u_{dc1} - u^*_{dc}\right) \\ \dot{u}_{cd1} = k_{pucd}\left(\dot{i}^*_{cd1} - \dot{i}_{cd1}\right) + k_{iucd}\left(i^*_{cd1} - i_{cd1}\right) \\ \dot{u}_{cq1} = k_{pucq}\left(0 - \dot{i}_{cq1}\right) + k_{iucq}\left(0 - i_{cq1}\right) \\ \dot{x}_{pll1} = \left(k_{\mathrm{ipll}}u_{tq1}\right)/\omega_0 \\ \dot{\varphi}_{pll1} = \omega_0\left(\left(k_{\mathrm{ppll}}u_{tq1}\right)/\omega_0 + x_{\mathrm{pll1}} - 1\right) \\ \dot{i}_{cd1} = \omega_0\left(u_{cd1} - u_{td1} + i_{cq1}X_f\right)/X_f \\ \dot{i}_{cq1} = \omega_0\left(u_{cq1} - u_{tq1} - i_{cd1}X_f\right)/X_f \\ \dot{u}_{dc1} = (P_{r1} - P_{c1})/(2Cu_{dc1}). \end{cases} \tag{B.19}$$

Combining (B.4), (B.12), (B.14), (B.16), and (B.18), the algebraic equations of the detailed model of the DFIG system are as follows:

$$\begin{cases} i_{rd1} = \left(X_m\psi_{sd1} - X_s\psi_{rd1}\right)/\left({X_m}^2 - X_rX_s\right) \\ i_{rq1} = \left(X_m\psi_{sq1} - X_s\psi_{rq1}\right)/\left({X_m}^2 - X_rX_s\right) \\ i_{sd1} = \left(X_r\psi_{sd1} - X_m\psi_{rd1}\right)/\left({X_m}^2 - X_rX_s\right) \\ i_{sq1} = \left(X_r\psi_{sq1} - X_m\psi_{rq1}\right)/\left({X_m}^2 - X_rX_s\right) \\ i_{td1} = i_{sd1} + i_{cd1} \\ i_{tq1} = i_{sq1} + i_{cq1} \\ u_{td1} = \left(\alpha_{\psi 1} + \alpha_{f1} + U_{g1}\cos\varphi_{\mathrm{pll1}} - i_{tq1}X_g\right)/\eta_\Sigma \\ u_{tq1} = \left(\beta_{\psi 1} + \beta_{f1} - U_{g1}\sin\varphi_{\mathrm{pll1}} + i_{td1}X_g\right)/\eta_\Sigma \\ U_{t1} = \sqrt{{u_{td1}}^2 + {u_{tq1}}^2} \\ P_{r1} = -u_{rd1}i_{rd1} - u_{rq1}i_{rq1} \\ P_{c1} = u_{cd1}i_{cd1} + u_{cq1}i_{cq1} \\ P_{t1} = u_{td1}i_{td1} + u_{tq1}i_{tq1}. \end{cases} \tag{B.20}$$

Similarly, in stage 2, the differential equations of the detailed model of the DFIG system are

$$\begin{cases} \dot{\psi}_{rd2} = \omega_0\left(u_{rd2} - R_ri_{rd2} + s_p\psi_{rq2}\right) \\ \dot{\psi}_{rq2} = \omega_0\left(u_{rq2} - R_ri_{rq2} - s_p\psi_{rd2}\right) \\ \dot{\psi}_{sd2} = \omega_0\left(u_{td2} + R_si_{sd2} - \omega_g\psi_{sq2}\right) \\ \dot{\psi}_{sq2} = \omega_0\left(u_{tq2} + R_si_{sd2} + \omega_g\psi_{sd2}\right) \\ \dot{u}_{rd2} = k_{purd}\left(0 - \dot{i}_{rd2}\right) + k_{iurd}\left(i^*_{rd2} - i_{rd2}\right) \\ \dot{u}_{rq2} = k_{purq}\left(0 - \dot{i}_{rq2}\right) + k_{iurq}\left(i^*_{rq2} - i_{rq2}\right) \\ \dot{i}^*_{cd2} = k_{pdc}\dot{u}_{dc2} + k_{idc}\left(u_{dc2} - u^*_{dc}\right) \\ \dot{u}_{cd2} = k_{pucd}\left(\dot{i}^*_{cd2} - \dot{i}_{cd2}\right) + k_{iucd}\left(i^*_{cd2} - i_{cd2}\right) \\ \dot{u}_{cq2} = k_{pucq}\left(0 - \dot{i}_{cq2}\right) + k_{iucq}\left(0 - i_{cq2}\right) \\ \dot{x}_{\mathrm{pll2}} = \left(k_{\mathrm{ipll}}u_{tq2}\right)/\omega_0 \\ \dot{\varphi}_{\mathrm{pll2}} = \omega_0\left(\left(k_{\mathrm{ppll}}u_{tq2}\right)/\omega_0 + x_{\mathrm{pll2}} - 1\right) \\ \dot{i}_{cd2} = \omega_0\left(u_{cd2} - u_{td2} + i_{cq2}X_f\right)/X_f \\ \dot{i}_{cq2} = \omega_0\left(u_{cq2} - u_{tq2} - i_{cd2}X_f\right)/X_f \\ \dot{u}_{dc2} = \left(P_{r2} - P_{c2}\right)/\left(2Cu_{dc2}\right). \end{cases} \tag{B.21}$$

The algebraic equations are

$$\begin{cases} i_{rq2}^{*} = K_e\left(U_{t2} - 0.9\right) + i_{rq1,s} \\ 0 \le i_{rd2}^{*} \le \sqrt{I_{\max}^2 - {i_{rq2}^{*}}^2} \\ i_{rd2} = \left(X_m\psi_{sd2} - X_s\psi_{rd2}\right) / \left({X_m}^2 - X_rX_s\right) \\ i_{rq2} = \left(X_m\psi_{sq2} - X_s\psi_{rq2}\right) / \left({X_m}^2 - X_rX_s\right) \\ i_{sd2} = \left(X_r\psi_{sd2} - X_m\psi_{rd2}\right) / \left({X_m}^2 - X_rX_s\right) \\ i_{sq2} = \left(X_r\psi_{sq2} - X_m\psi_{rq2}\right) / \left({X_m}^2 - X_rX_s\right) \\ i_{td2} = i_{sd2} + i_{cd2} \\ i_{tq2} = i_{sq2} + i_{cq2} \\ u_{td2} = \left(\alpha_{\psi 2} + \alpha_{f2} + U_{g2}\cos\varphi_{\text{pll}2} - i_{tq2}X_g\right)/\eta_{\Sigma} \\ u_{tq2} = \left(\beta_{\psi 2} + \beta_{f2} - U_{g2}\sin\varphi_{\text{pll}2} + i_{td2}X_g\right)/\eta_{\Sigma} \\ U_{t2} = \sqrt{{u_{td2}}^2 + {u_{tq2}}^2} \\ P_{r2} = -u_{rd2}i_{rd2} - u_{rq2}i_{rq2} \\ P_{c2} = u_{cd2}i_{cd2} + u_{cq2}i_{cq2}. \end{cases} \tag{B.22}$$

Similarly, in stage 3, the differential equations of the detailed model of the DFIG system are

$$\begin{cases} \dot{\psi}_{rd3} = \omega_0\left(u_{rd3} - R_ri_{rd3} + s_p\psi_{rq3}\right) \\ \dot{\psi}_{rq3} = \omega_0\left(u_{rq3} - R_ri_{rq3} - s_p\psi_{rd3}\right) \\ \dot{\psi}_{sd3} = \omega_0\left(u_{td3} + R_si_{sd3} - \omega_g\psi_{sq3}\right) \\ \dot{\psi}_{sq3} = \omega_0\left(u_{tq3} + R_si_{sd3} + \omega_g\psi_{sd3}\right) \\ \dot{i}_{rd3}^{*} = K_{\text{ramp}} \\ \dot{i}_{rq3}^{*} = k_{pV}\dot{U}_{t3} + k_{iV}(U_{t3} - {U_t}^{*}) \\ \dot{u}_{rd3} = k_{purd}\left(\dot{i}_{rd3}^{*} - \dot{i}_{rd3}\right) + k_{iurd}\left(i_{rd3}^{*} - i_{rd3}\right) \\ \dot{u}_{rq3} = k_{purq}\left(\dot{i}_{rq3}^{*} - \dot{i}_{rq3}\right) + k_{iurq}\left(i_{rq3}^{*} - i_{rq3}\right) \\ \dot{i}_{cd3}^{*} = k_{pdc}\dot{u}_{dc3} + k_{idc}\left(u_{dc3} - u_{dc}^{*}\right) \\ \dot{u}_{cd3} = k_{pucd}\left(\dot{i}_{cd3}^{*} - \dot{i}_{cd3}\right) + k_{iucd}\left(i_{cd3}^{*} - i_{cd3}\right) \\ \dot{u}_{cq3} = k_{pucq}\left(0 - \dot{i}_{cq3}\right) + k_{iucq}\left(0 - i_{cq3}\right) \\ \dot{x}_{\text{pll}3} = \left(k_{i\text{pll}}u_{tq3}\right)/\omega_0 \\ \dot{\varphi}_{\text{pll}3} = \omega_0\left(\left(k_{p\text{pll}}u_{tq3}\right)/\omega_0 + x_{\text{pll}3} - 1\right) \\ \dot{i}_{cd3} = \omega_0\left(u_{cd3} - u_{td3} + i_{cq3}X_f\right)/X_f \\ \dot{i}_{cq3} = \omega_0\left(u_{cq3} - u_{tq3} - i_{cd3}X_f\right)/X_f \\ \dot{u}_{dc3} = \left(P_{r3} - P_{c3}\right)/\left(2Cu_{dc3}\right). \end{cases} \tag{B.23}$$

The algebraic equations are

$$\begin{cases} i_{rd3} = \left(X_m\psi_{sd3} - X_s\psi_{rd3}\right) / \left({X_m}^2 - X_rX_s\right) \\ i_{rq3} = \left(X_m\psi_{sq3} - X_s\psi_{rq3}\right) / \left({X_m}^2 - X_rX_s\right) \\ i_{sd3} = \left(X_r\psi_{sd3} - X_m\psi_{rd3}\right) / \left({X_m}^2 - X_rX_s\right) \\ i_{sq3} = \left(X_r\psi_{sq3} - X_m\psi_{rq3}\right) / \left({X_m}^2 - X_rX_s\right) \\ i_{td3} = i_{sd3} + i_{cd3} \\ i_{tq3} = i_{sq3} + i_{cq3} \\ u_{td3} = \left(\alpha_{\psi 3} + \alpha_{f3} + U_{g3}\cos\varphi_{pll3} - i_{tq3}X_g\right)/\eta_{\Sigma} \\ u_{tq3} = \left(\beta_{\psi 3} + \beta_{f3} - U_{g3}\sin\varphi_{pll3} + i_{td3}X_g\right)/\eta_{\Sigma} \\ U_{t3} = \sqrt{{u_{td3}}^2 + {u_{tq3}}^2} \\ P_{r3} = -u_{rd3}i_{rd3} - u_{rq3}i_{rq3} \\ P_{c3} = u_{cd3}i_{cd3} + u_{cq3}i_{cq3}. \end{cases} \tag{B.24}$$

In the above-mentioned models, the differences among various stages lie in the fact that the MSC implements different outer-loop controls, as shown in Fig. 2, while the other parts remain consistent.

REFERENCES

[1] M. Liserre, R. Cardenas, M. Molinas, and J. Rodriguez, "Overview of multi-MW wind turbines and wind parks," *IEEE Trans. Ind. Electron.*, vol. 58, no. 4, pp. 1081–1095, Apr. 2011.

[2] E. O. N. GmbH, *Grid Code-High and Extra High Voltage.* Bayreuth, Germany, 2006. [Online]. Available: https://wenku.baidu.com/view/9ca75c8ecc22bcd126ff0c4b.html

[3] *Technical Rule for Connecting Wind Farm to Power System,* Chinese Standard: GB/T19963-2011, China Electric Power Press, Beijing, China, 2011.

[4] O. P. Mahela, N. Gupta, M. Khosravy, and N. Patel, "Comprehensive overview of low voltage ride through methods of grid integrated wind generator," *IEEE Access*, vol. 7, pp. 99299–99326, 2019.

[5] R. Ma, Y. Zhang, M. Han, J. Kurths, and M. Zhan, "Synchronization stability and multi-timescale analysis of renewable-dominated power systems," *Chaos: An Interdiscipl. J. Nonlinear Sci.*, vol. 33, no. 8, 2023, Art. no. 082101.

[6] Y. Zhang, M. Han, and M. Zhan, "The concept and understanding of synchronous stability in power electronic-based power systems," *Energies*, vol. 16, no. 6, 2023, Art. no. 2923.

[7] W. Tang, J. Hu, Y. Chang, and F. Liu, "Modeling of DFIG-based wind turbine for power system transient response analysis in rotor speed control timescale," *IEEE Trans. Power Syst.*, vol. 33, no. 6, pp. 6795–6805, Nov. 2018.

[8] X. He, H. Geng, J. Xi, and J. M. Guerrero, "Resynchronization analysis and improvement of grid-connected VSCs during grid faults," *IEEE Trans. Emerg. Sel. Topics Power Electron.*, vol. 9, no. 1, pp. 438–450, Feb. 2021.

[9] Ö. Göksu, R. Teodorescu, C. L. Bak, F. Iov, and P. C. Kjær, "Instability of wind turbine converters during current injection to low voltage grid faults and PLL frequency based stability solution," *IEEE Trans. Power Syst.*, vol. 29, no. 4, pp. 1683–1691, Jul. 2014.

[10] X. He, H. Geng, R. Li, and B. C. Pal, "Transient stability analysis and enhancement of renewable energy conversion system during LVRT," *IEEE Trans. Sustain. Energy*, vol. 11, no. 3, pp. 1612–1623, Jul. 2020.

[11] R. Ma, J. Li, J. Kurths, S. Cheng, and M. Zhan, "Generalized swing equation and transient synchronous stability with PLL-based VSC," *IEEE Trans. Energy Convers.*, vol. 37, no. 2, pp. 1428–1441, Jun. 2022.

[12] M. Han, R. Ma, and M. Zhan, "Transient synchronous stability analysis and assessment of PLL-based VSC systems by bifurcation theory," *IEEE Trans. Energy Convers.*, vol. 40, no. 2, pp. 1312–1324, Jun. 2025.

[13] M. Zarif Mansour, M. Si Phu, S. Hadavi, B. Badrzadeh, A. Karimi, and B. Bahrani, "Nonlinear transient stability analysis of phased-locked loop-based grid-following voltage-source converters using lyapunov's direct method," *IEEE Trans. Emerg. Sel. Topics Power Electron.*, vol. 10, no. 3, pp. 2699–2709, Jun. 2022.

[14] Q. Hu, L. Fu, F. Ma, and F. Ji, "Large signal synchronizing instability of PLL-based VSC connected to weak AC grid," *IEEE Trans. Power Syst.*, vol. 34, no. 4, pp. 3220–3229, Jul. 2019.

[15] H. Wu and X. Wang, "Design-oriented transient stability analysis of PLL-synchronized voltage-source converters," *IEEE Trans. Power Electron.*, vol. 35, no. 4, pp. 3573–3589, Apr. 2020.

[16] Z. Li, J. Li, D. Gan, and Z. Wang, "Stability analysis of PLL-type grid-connected converter based on the perturbation method," *IEEE Trans. Power Del.*, vol. 39, no. 2, pp. 1151–1161, Apr. 2024.

[17] T. Wu, Q. Jiang, M. Huang, and X. Xie, "Synchronization stability of grid-following converters governed by saturation nonlinearities," *IEEE Trans. Power Syst.*, vol. 37, no. 5, pp. 4102–4105, Sep. 2022.

[18] Y. Li, Y. Tang, Y. Lu, F. Hua, and Z. Du, "Synchronization stability of grid-connected VSC with limits of PLL," *IEEE Trans. Power Syst.*, vol. 38, no. 4, pp. 3965–3976, Jul. 2023.

[19] P. Chao, W. Li, and X. Liang, "An analytical two-machine equivalent method of DFIG-based wind power plants considering complete FRT processes," *IEEE Trans. Power Syst.*, vol. 36, no. 4, pp. 3657–3667, Jul. 2021.

[20] W. Li, P. Chao, and X. Liang, "An improved single-machine equivalent method of wind power plants by calibrating power recovery behaviors," *IEEE Trans. Power Syst.*, vol. 33, no. 4, pp. 4371–4381, Jul. 2018.

[21] J. J. Sanchez-Gasca, "Generic wind turbine generator models for WECC-a second status report," in *Proc. IEEE Power Energy Soc. Gen. Meeting*, 2015, pp. 1–5.

[22] K. Clark, N. W. Miller, and J. J. Sanchez-Gasca, "Modeling of GE wind turbine-generators for grid studies," in *GE Energy*, vol. 4, pp. 885–8950, 2010.

[23] L. Tang, C. Shen, and X. Zhang, "Impact of large-scale wind power centralized integration on transient angle stability of power systems—Part I: Theoretical foundation," *Proc. CSEE*, vol. 35, no. 16, pp. 4043–4051, 2015.
[24] M. Arani and Y. Mohamed, "Analysis and mitigation of undesirable impacts of implementing frequency support controllers in wind power generation," *IEEE Trans. Energy Convers.*, vol. 31, no. 1, pp. 174–186, Mar. 2016.
[25] J. Pei, J. Yao, Y. Liu, S. Chen, P. Sun, and S. Huang, "Modeling and transient synchronization stability analysis for PLL-based renewable energy generator considering sequential switching schemes," *IEEE Trans. Power Electron.*, vol. 37, no. 2, pp. 2165–2179, Feb. 2022.
[26] W. Ding, H. Geng, B. Ren, Q. Li, and R. Sun, "Analytical switching modeling method of grid-connected converters for transient stability analysis," *IEEE Trans. Ind. Appl.*, vol. 60, no. 5, pp. 7511–7521, Sep./Oct. 2024.
[27] Y. Zhang and M. Zhan, "Transient synchronous stability analysis of PMSG grid-connected system considering transient switching control under severe faults," *IEEE Trans. Power Electron.*, vol. 40, no. 5, pp. 7298–7314, May 2025.
[28] J. Hu, X. Yuan, and S. Cheng, "Multi-time scale transients in power-electronized power systems considering multi-time scale switching control schemes of power electronics apparatus," *Proc. CSEE*, vol. 39, no. 18, pp. 5457–5467, 2019.
[29] Y. Han, Y. Feng, P. Yang, L. Xu, Y. Xu, and F. Blaabjerg, "Cause, classification of voltage sag, and voltage sag emulators and applications: A comprehensive overview," *IEEE Access*, vol. 8, pp. 1922–1934, 2020.
[30] G. Abad et al., *Doubly Fed Induction Machine: Modeling and Control for Wind Energy Generation*. Hoboken, NJ, USA: Wiley, 2011.
[31] U. Buragohain, A. S. Mir, and N. Senroy, "Adequacy of reduced-order DFIG models for dynamic stability assessment," *IEEE Trans. Circuits Syst. I: Reg. Papers*, vol. 72, no. 7, pp. 3706–3717, Jul. 2025.
[32] B. Wu, Y. Lang, N. Zargai, and S. Kouro, *Power Conversion and Control of Wind Energy Systems*. Hoboken, NJ, USA: Wiley, 2011.
[33] Z. Yang, R. Ma, S. Cheng, and M. Zhan, "Nonlinear modeling and analysis of grid-connected voltage-source converters under voltage dips," *IEEE Trans. Emerg. Sel. Topics Power Electron.*, vol. 8, no. 4, pp. 3281–3292, Dec. 2020.
[34] X. Han, B. Jiang, and Q. Bi, "Symmetric bursting of focus–focus type in the controlled lorenz system with two time scales," *Phys. Lett. A*, vol. 373, no. 40, pp. 3643–3649, 2009.

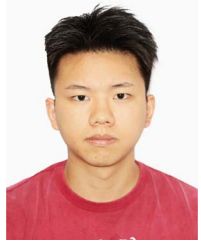

Hongsheng Xu received the B.S. degree in electrical engineering and automation from North China Electric Power University, Baoding, China, in 2022. He is currently working toward the Ph.D. degree in electrical engineering with the School of Electrical and Electronic Engineering, Huazhong University of Science and Technology, Wuhan, China.

His research interests include the transient stability of renewable dominated power systems.

Meng Zhan (Senior Member, IEEE) was born in Jingdezhen, Jiangxi, China, in 1974. He received the B.S. degree in physics and the Ph.D. degree in nonlinear physics from Beijing Normal University, Beijing, China, in 1996 and 2001, respectively.

From 2001 to 2006, he was a Postdoctoral Researcher with the National University of Singapore, Singapore, and University of Toronto, Toronto, ON, Canada. Since 2006, he has been a Full Professor with the Wuhan Institute of Physics and Mathematics, Chinese Academy of Sciences, Wuhan, China. Since 2015, he has been with the State Key Laboratory of Advanced Electromagnetic Engineering and Technology, School of Electrical and Electronic Engineering, Huazhong University of Science and Technology, Wuhan, China. He has long been engaged in the study of nonlinear dynamics of complex systems in multiple directions, such as coupled nonlinear systems, chaos synchronization and control, pattern formation, and complex network dynamics. He has authored or coauthored over 120 SCI papers in internationally peer-reviewed journals, which have been cited more than 3000 times. His H-index is 32. His research interests include power-electronic-based power system dynamics, renewable dominated power system stability, and nonlinear analysis of power system.